Results in Engineering 26 (2025) 105061

Contents lists available at ScienceDirect

Results in Engineering

journal homepage: www.sciencedirect.com/journal/results-in-engineering

Research paper

Passive control of sonic flow from converging nozzle with D-shaped rib

Mayur Bharatbhai Makwana [a], Sayed Ahmed Imran Bellary [a], Sher Afghan Khan [b], Abdul Aabid [c,*], Muneer Baig [c]

[a] Department of Space, School of Engineering, Ajeenkya DY Patil University, Pune, Maharashtra, India
[b] Department of Mechanical & Aerospace Engineering, Faculty of Engineering, IIUM, Kuala Lumpur, Malaysia
[c] Department of Engineering Management, College of Engineering, Prince Sultan University, PO BOX 66833, Riyadh 11586, Saudi Arabia

ARTICLE INFO

Keywords:
Circular ribs
CFD
Flow control
Mach number
Duct

ABSTRACT

The abrupt expansion at the blunt base of projectiles, rockets, missiles, etc., is a common phenomenon. Flow separation and reattachment are caused by the abrupt increase in the base area, and the pressure in the separated recirculation area is lower than the surrounding atmospheric pressure. The separation at the blunt base will result in low pressure, resulting in a considerable amount of the base drag. In this work, the base pressure, which is lower than the ambient pressure leading to base drag, which is significant at the critical Mach numbers, is controlled by a passive control method such as a d-shaped rib. The duct diameter is 25 mm, and its length-to-diameter (L/D) ratio is 6. Ribs of heights ranging from 1 mm to 3 mm ribs were utilized to control the base pressure when located at L/D = 0.5, 1.0, 1.5, 2, and 3. When the rib was located at L/D = 1, the base pressure values for 3 mm rib height considerably increased the base pressure. The ribs with smaller heights are more vulnerable to changes in rib placements since the reattachment point is between L/D = 2 and 3D That results in slight variations in the base pressure ratios at other locations. According to the study, 2 mm ribs are the optimum option if the mission requires equating the base pressure to ambient atmospheric pressure. If the mission requires a fifty percent enhancement in base pressure, then even a 1 mm rib is sufficient. The 3 mm rib is the optimum option if the mission requirements call for raising the base pressure considerably.

1. Introduction

Ever since fluid science study began, turbulence has been a mystery. We must comprehend turbulence because it is a part of almost every technical and natural activity in our environment at high-speed flow. Drag is associated with turbulent flows; we need a fair idea of turbulence to control drag. Specific fluxes, including those involving the mixing of fluids, require turbulence. Conversely, turbulence is unwanted and should be controlled in industrial applications with the least energy input. In engineering and real-world flows, turbulent drag has a noteworthy financial and ecological impact. That is mainly because of the combustion byproducts and the fossil petroleum used in numerous transportation kinds, which contribute to nearly 20% of total emissions.

An essential problem with many applications is unexpected flow expansion in subsonic and supersonic regimes. When used as a supersonic parallel diffuser, a jet and shroud configuration is an excellent method for resolving unexpected expansion issues. Another interesting application for the system that replicates high altitude conditions in test cells for rocket and jet engines is a jet releasing into a shroud and generating a high enough subatmospheric discharge pressure. The flow state of the exhaust port of an internal combustion engine is similar; a jet of hot exhaust gases passes through the exhaust valve. Another relevant instance where the flow grows interiorly rather than away from the axis of symmetry, as in the previous situation, is when the flow goes inward to the blunt base of a projectile in flight.

The flow parting, recirculation, and reattachment are characteristics of the intricate phenomena known as the abrupt axisymmetric expansion flow field. As shown in Fig. 1(a), such a flow can split into two core regions—the central flow section and the flow recirculation region—by a dividing streamline, also known as a dividing surface. The reattachment point is the location where the wall and dividing streamline meet. The distance between the reattachment point and the base is known as the reattachment distance. The duct area, expansion level, nozzle exit Mach number, and the reattachment length are the variables that will fix the base pressure values. The reattachment distance will depend on the

---

* Corresponding author.

E-mail addresses: mayurmb300@gmail.com (M.B. Makwana), ibellary@gmail.com (S.A.I. Bellary), sakhan@iium.edu.my (S.A. Khan), aaabid@psu.edu.sa (A. Aabid), mbaig@psu.edu.sa (M. Baig).

https://doi.org/10.1016/j.rineng.2025.105061
Received 27 February 2025; Received in revised form 4 April 2025; Accepted 22 April 2025

Nomenclature

A_1	Nozzle Exit Area
A_2	Duct Exit Area
A_2/A_1	Area Ratio
M	Mach Number
L/D	Length-to-diameter Ratio
P_a	Ambient/atmospheric Pressure
P_e	Pressure at the exit of the nozzle
P_w	Wall Pressure inside the Duct
ρ	Air Density
μ	Air Viscosity
μo	Reference Viscosity
T	Static Temperature
T_o	Reference Static Temperature (in K)
S	Sutherland Constant
k	Thermal Conductivity
Cp	Specific heat capacity
a	Velocity of sound
P_{inlet}	Inlet Pressure
P_{outlet}	Outlet Pressure
P_{gauge}	Gauge Pressure
P_o	Stagnation Pressure in Settling Chamber
P_b/P_a	Non-dimensional Base Pressure Ratio
P_w/P_a	Non-dimensional Wall Pressure Ratio
σk	Turbulent Prandtl number
ε	Turbulent kinetic energy dissipation rate
$C\mu$	Arbitrary Constant
C1	Arbitrary Constant
C2	Arbitrary Constant
$f\mu$	Arbitrary Constant
$\sigma\varepsilon$	Arbitrary Constant
v	Velocity
μt	Turbulent Viscosity
Prt	Turbulent Prandtl number
L	Length of the enlarged duct
D	Diameter of the enlarged duct
Di	Nozzle inlet diameter
w	Width of the rib
h	Height of the rib
r	Rib Radius
Re	Reynolds number
RAP	Reattachment point
RAL	Reattachment length

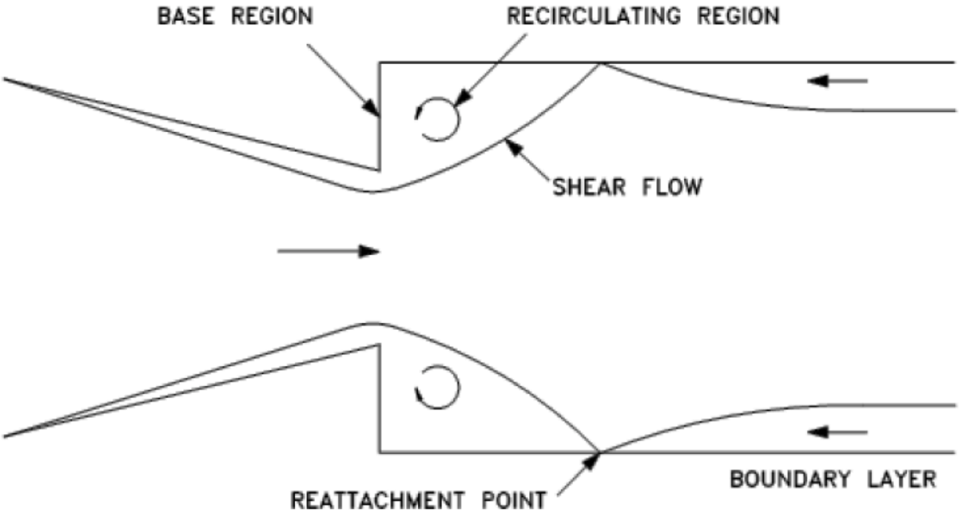

(a)

Fig. 1. (a) Sudden Expansion Flow Field.

consequence of the base pressure, duct diameter, and the degree of expansion.

Given its size and influence on the performance of the weapon systems in terms of the range of the missiles, rockets, bombs, and projectiles, the base drag contributes significantly. It can account for up to 2/3rd of the total drag for airplane fuselage. Even a slight increase in base pressure will be very beneficial, as this will enhance the net range of aircraft, reduce the need for fossil fuels, and ultimately lessen global warming. One of the most critical areas for researchers is base pressure control. Imagine the application is in artillery rounds, unguided rockets, and external flow-over missiles. The base drag component would be essentially zero as we strive to raise the base pressure equal to the atmospheric pressure. Jet-on conditions, however, will eliminate the base drag component, such as that of missiles and unguided rockets. This jet-on time is typically relatively short compared to the whole flight duration. Because launch vehicles have a very long total flight period, the propulsion system is discarded after each stage to prevent the dead weight of the propulsion unit from being carried. Nevertheless, since having a discarding mechanism is not a cost-effective option for short-range unguided rockets, the dead weight of the propulsion unit remains attached to the weapon system.

If the purpose is for a propulsion system of a combustion chamber, we want the base pressure to be as low as possible. That will ensure good fuel and air mixing and improve combustion efficiency. Therefore, the goal of this investigation is to control the base pressure. The application will determine whether the mission requires increasing or decreasing the base pressure. This study is a technology demonstration, and the mission requirements will determine the final geometrical and flow

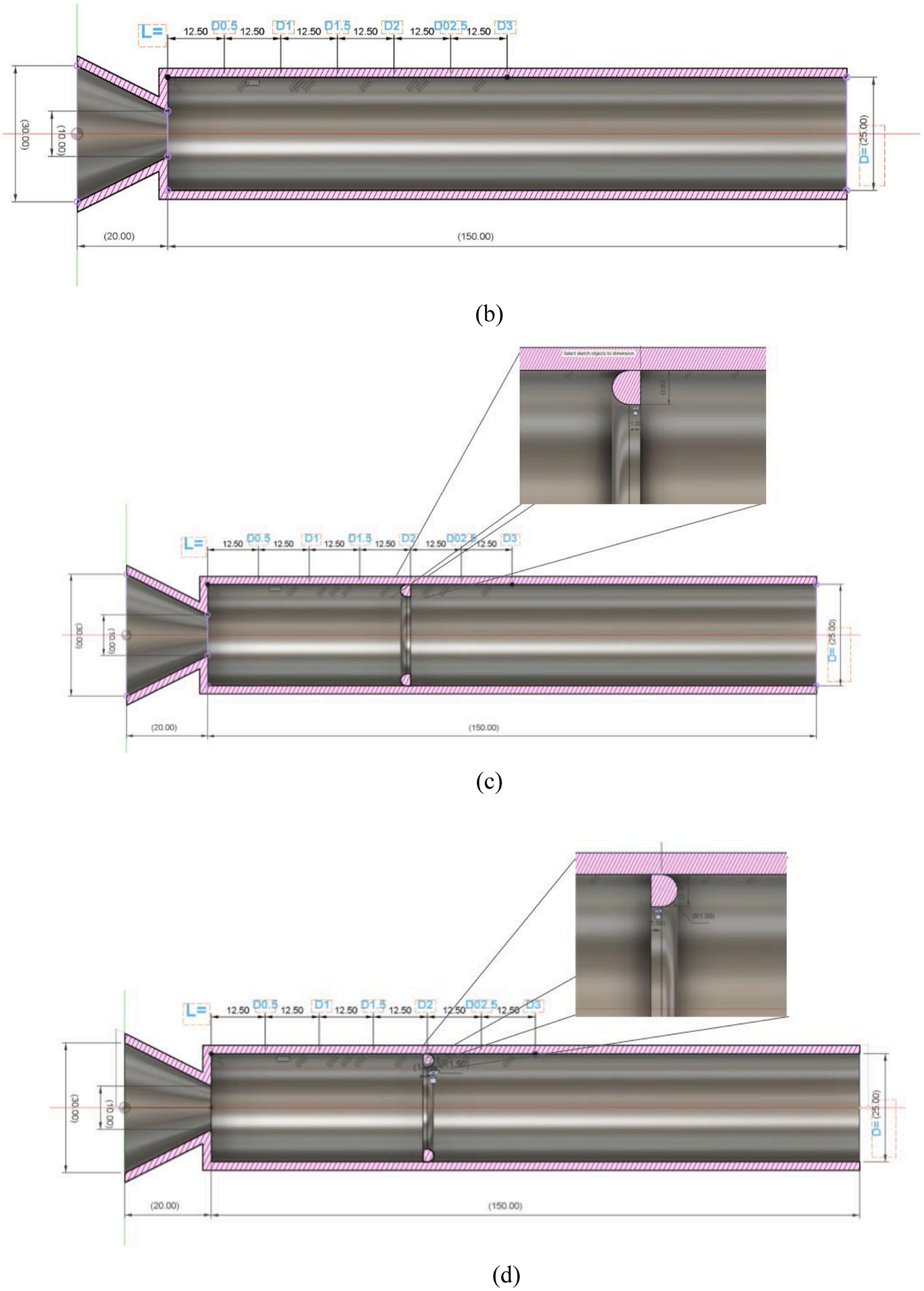

Fig. 1. (b to d) Sonic nozzle with sudden expansion circular duct (b) without control, (c) with d-shape Rib Orientation 1 control, and (d) with d-shape Rib Orientation 2 control.

characteristics.

2. Literature review

The efficiency of quarter ribs in regulating base pressure in a sudden expansion duct at sonic Mach numbers was examined by Khan et al. [1] using a thorough CFD analysis. Their research showed that altering the recirculation zone improved pressure recovery, reducing drag and adding ribs to increase the base pressure. The impact of ribs on abruptly expanded flows at sonic Mach values was further investigated by Khan et al. [2]. They discovered that well-positioned ribs along the duct walls improved pressure distribution, decreased aerodynamic drag, and efficiently managed flow separation. Husnina et al. [3] conducted passive base pressure flow control in a C-D nozzle with an area ratio of 2.56 at Mach 1.8. The study showed that passive control strategies, including nozzle exit Mach number and surface modifications inside the duct, improved pressure recovery while preserving flow stability. Semi-circular ribs were first used by Khan et al. [4] to mimic base flow as a novel method of controlling base pressure at critical Mach numbers. According to their research, semi-circular ribs enhanced aerodynamic performance by successfully reducing shock-induced flow separation. A thorough CFD study of the effect of splitter plates on bluff bodies was conducted by Aabid et al. [5]. According to their findings, splitter plates improved overall flow characteristics and decreased drag by reducing the wake zone behind the body.

Rectangular ribs were used to control nozzle flow at sonic and supersonic Mach values, according to Sethuraman et al. [6]. According to the study, the rectangular ribs significantly improved flow homogeneity and pressure recovery. Kadivar et al. [7] examined different approaches to forecast turbulent flow and heat transfer in wavy and smooth channels, including Reynolds-averaged and Navier-Stokes (RANS) models. The k-ε model produced the most accurate findings for complex flow conditions. Orlandi et al. [8] used CFD tools to study cavitation analysis in industrial pumps. Their research highlighted how crucial accurate cavitation modeling is to forecasting pump performance and preventing damage. Passive fuel injection approaches in scramjet combustors were studied by Bordoloi et al. [9]. They discovered that passive injection enhanced stable flame propagation and combustion efficiency by improving fuel-air mixing. A study by Gahlot et al. [10] examined how turbulence modeling affected the efficiency of mixed compression supersonic air intakes. Their results showed that precise turbulence models greatly enhanced flow homogeneity and intake efficiency.

The impact of boattail angles on drag and pressure distribution for axisymmetric afterbodies at low speeds was investigated by Ambo et al. [11]. The findings demonstrated that enhanced aerodynamic performance and reduced pressure drag were achieved by optimizing boattail angles. Viswanath thoroughly examined flow control strategies for base drag reduction [12]. The study emphasized successful tactics, such as geometric adjustments and passive flow control devices. Perry examined base pressure parameters in simplified automotive squareback geometries [13]. The study found that aerodynamic drag and base pressure were significantly affected by geometric changes. For a cavity flow at Mach 1.5, Aradag et al. [14] investigated dynamic and passive control strategies. According to their findings, hybrid control strategies performed better at minimizing flow-induced pressure variations. Mousavi and Roohi examined three-dimensional shock train configurations in convergent-divergent nozzles [15]. Their analysis identified critical parameters affecting shock train development and flow stability.

Using CFD, Rao et al. [16] examined the flow properties in convergent-divergent nozzles. Their results underlined how crucial precise boundary conditions are to trustworthy flow forecasts. The K-ε and Spalart-Allmaras turbulence models for flow where there is a change in the air density via convergent-divergent nozzles were compared by Najar et al. [17]. The study found that the K-ε model more accurately predicted flow and reattachment. Salvador et al. [18] investigated cavitation patterns in diesel injector convergent-divergent nozzles using a homogeneous equilibrium model. Their findings demonstrated how crucial cavitation modeling is to injector performance and design. Pushpa et al. [19] investigated heat dissipation and buoyant convective flow in Cu–H2O nanoliquids inside an annulus via a thin baffle. The study showed that using nanoliquid improved heat transfer performance. Koomullil et al. [20] suggested a thorough generalized mesh framework for CFD applications. Their method made it possible to simulate intricate flow conditions and geometries accurately.

Marzougui et al. [21] examined heat transport and entropy production in Cu–water nano liquids inside porous lid-driven cavities under magnetic fields. Their results demonstrated the significance of external fields in enhancing heat transfer efficiency. Pandey and Rathakrishnan [22] studied using annular chambers for base flow control. The study showed that annular cavities effectively reduced base drag by changing the recirculation zone. Tu et al. [23] offered a practical approach to computational fluid dynamics, focusing on best practices for accurate simulations and flow analysis. Essential concepts and analytical methods for compressible fluid flow were introduced by Oosthuizen and Carscallen [24]. Their work is a fundamental reference for CFD mechanical and aeronautical engineering applications.

Rathakrishnan [25] experimented with controlling the base pressure in an abruptly expanded tube using five ribs with width-to-height ratios of 3:1, 3:2, and 3:3. NPRs ranging from 1.141, 1.295, 1.550, 1.707, and 2.458 were tested, along with nozzle exit Mach numbers of 0.44, 0.62, 0.82, 0.91, and 1.0. According to experimental data, the control lowers the base pressure for lower aspect ratios of the ribs, specifically 3:1 and 3:2. Nonetheless, the base pressure rose when ribs with a 3:3 aspect ratio were employed to control the flow. In the present study, Rathakrishnan [25] results are considered benchmark data for validating the CFD results. The authors believe one rib can be enough to achieve the intended effects rather than five.

This literature overview highlights significant developments in base pressure control, turbulence modeling, and CFD-based flow optimization. As far as the author knows, d-shaped ribs have not been used in research. Regarding the experimental study, researchers have used rectangular ribs in the literature to control the base pressure in a circular pipe and the square duct. Another study was conducted where a semi-circular rib was considered to regulate the base flows. However, semi-circular ribs were not very effective.

Regarding the CFD simulations, few researchers have used triangular, semi-circular, and rectangular ribs in square ducts at sonic and supersonic Mach numbers. The studies show how active and passive control strategies can improve aerodynamic performance while lowering flow instability and drag. Based on the above review, we can state that this study will add additional information to the scientific literature and will be helpful in the design of aerospace vehicles.

3. Problem formulation

A two-dimensional sonic nozzle with a suddenly expanded duct has been defined. Flow conditions are measured based on the sonic Mach number. The sudden expansion duct is analyzed in three categories: (1) without control of the sonic flow, (2) control of the sonic flow with orientation 1 of the d-shaped rib, and (3) control of the sonic flow with orientation 2 of the d-shaped rib. These orientations have been altered because the d-shaped ribs involve modifications in design, making it essential to understand how the control mechanism behaves for different orientations. Further investigations are conducted by varying the location of the d-shaped ribs for different rib geometry and flow conditions. The key parameters considered in this investigation are the Mach number, rib location, duct diameter, rib orientation, and the nozzle pressure ratio (NPR). Fig. 1(b) illustrates the nozzle and duct assembly with a plain duct. Fig. 1(c) shows the nozzle assembly with a d-shaped rib in orientation 1, where the curved part faces the base region. Fig. 1(d) represents orientation 2, where the straight part of the d-shaped rib faces the base region. In both orientations, the base pressure

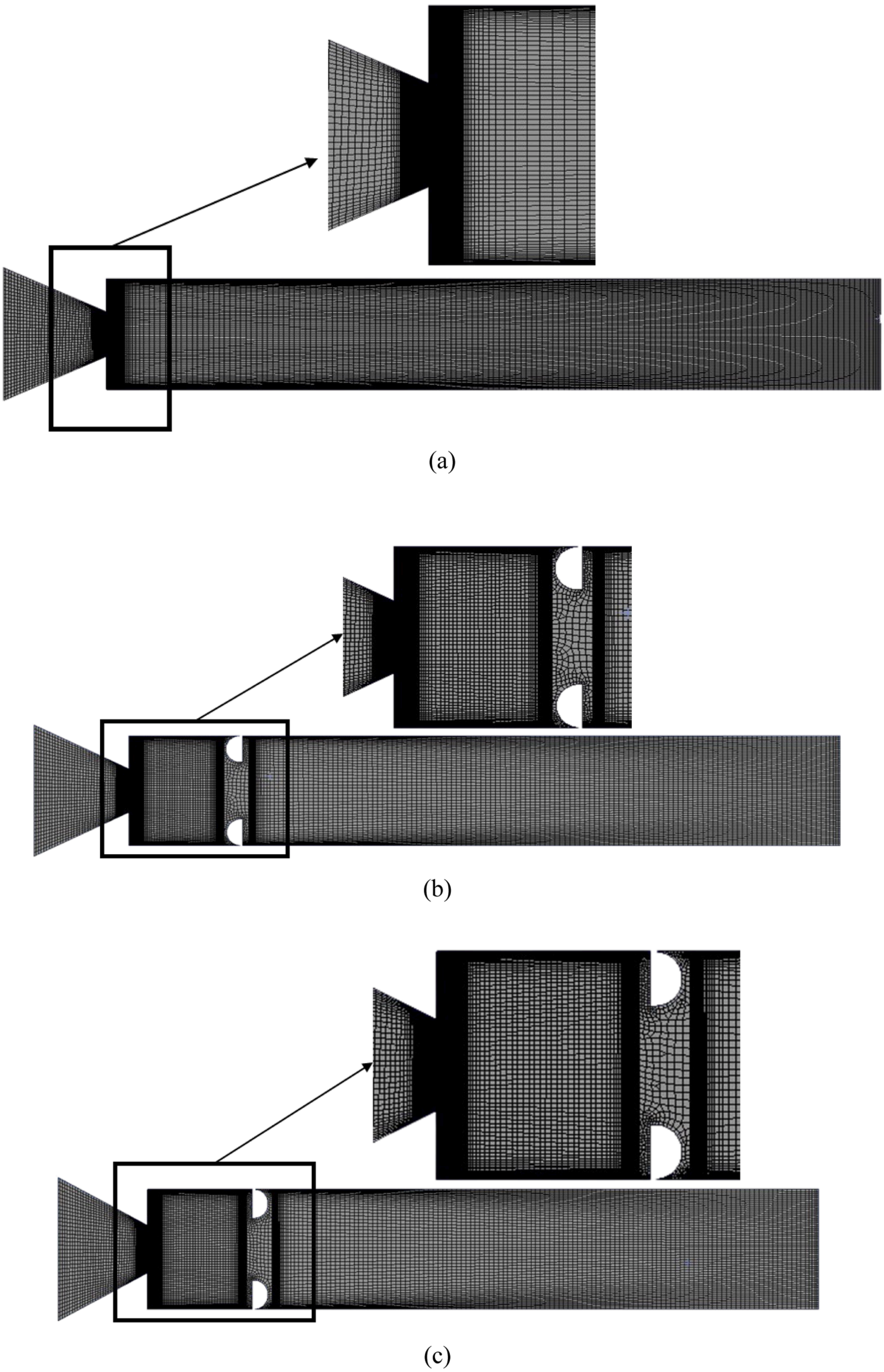

Fig. 2. Mesh model (a) without control (b) with control orientation 1 (c) with control orientation 2.

results are expected to differ due to the different geometrical configurations of the d-shaped rib interacting with the base zone.

4. Computational fluid dynamics

4.1. Governing equations

Consideration is given to the following theories:

i. The flow is turbulent; hence, viscous dissipation effects are considered.
ii. The fluid is compressible, and its viscosity changes with temperature.
iii. The flow turns off the duct at atmospheric pressure.
iv. We looked through the literature and discovered that the internal flow k-epsilon turbulence model is the best because it produces promising findings.

The formula for Sutherland's three-coefficient viscosity model is shown in Eq. (1).

$$\mu' = \mu'_o \left(\frac{T_a}{T_{a,\,o}}\right)^{3/2} \frac{T_{a,\,o} + S'}{T_a + S'} \tag{1}$$

With μ' stands for viscosity, the reference viscosity value in kg/m-s is expressed as μ'_o. T_a stands for static temperature, K for standard reference temperature, and S' for temperature-reliant Sutherland coefficient.

The following is the equation for mass balance:

$$\frac{\partial \rho}{\partial t} + \underline{\nabla}\cdot\left(\rho \underline{V}\right) = 0 \tag{2}$$

Where the fluid's velocity is denoted by V. The equation for momentum balance is:

$$\frac{\partial}{\partial t}\left(\rho \underline{V}\right) + \underline{\nabla}\cdot\left(\rho \underline{V}\underline{V}\right) + \underline{\nabla} p = \underline{\nabla}\cdot\left[2\mu\left(\underline{\nabla}\underline{V}\right)_o^s\right] + \underline{\nabla}\cdot(\tau_{=Re}) \tag{3}$$

Where $(\underline{\nabla}\underline{V})_o^s = (\underline{\nabla}\underline{V})^s - \frac{1}{3}(\underline{\nabla}\cdot\underline{V})\underline{I}$, $(\underline{\nabla}\underline{V})^s = \frac{\nabla V + \nabla V^T}{2}$ and $\tau_{=Re}$ is the turbulent stress tensor. The formulae for total energy are as follows:

$$\frac{\partial}{\partial t}\left[\rho\left(\frac{1}{2}V^2 + u_{int}\right)\right] + \underline{\nabla}\left[\rho\left(\frac{1}{2}V^2 + u_{int}\right)\underline{V}\right]$$
$$= \underline{\nabla}\left(\lambda\underline{\nabla}T - p\underline{V} + 2\mu\underline{V}\cdot\left(\underline{\nabla}\underline{V}\right)_o^s + \underline{V}\cdot\tau_{=Re}\right) \tag{4}$$

Thermal conductivity is denoted by λ and internal energy by u_{int}; the k-epsilon turbulence model is utilized in internal flow simulations because of its cost, robustness, and precision. The Ansys Fluent integrates this study's k-epsilon (ε) turbulence model. The turbulent kinetic energy was computed using the K-equation.

$$\frac{\partial}{\partial t}(\rho k) + \underline{\nabla}\cdot\left(\rho\underline{V}k\right) = \underline{\nabla}\cdot\left[\left(\mu + \frac{\mu_t}{\sigma_k}\right)\left(\underline{\nabla}k\right)\right] - \rho\varepsilon + M_x \tag{5}$$

The turbulent kinetic energy indulgence rate is designated by ε, the turbulent Prandtl number is $\sigma - k$, and the word Mx is the turbulence generation. Precisely, the dissipation (or (-equation)) is controlled by,

$$\frac{\partial(\rho\varepsilon)}{\partial t} = -\underline{\nabla}\cdot\left(\rho\varepsilon\overrightarrow{V}\right) + \underline{\nabla}\cdot\left[\left(\mu + \frac{\mu_T}{\sigma_\varepsilon}\right)\nabla\varepsilon\right] - C_1 f_1\left(\frac{\varepsilon}{k}\right)M - C_2 f_2\frac{\varepsilon^2}{k} \tag{6}$$

where $\mu_t = \rho f_\mu C_\mu k^2/\varepsilon$ denotes turbulent viscosity, and the random constants are represented as $\overline{C_\mu} = 0.09$, $\overline{C_1} = 1.44$, $\overline{C_2} = 1.92$, $\overline{f_\mu} = 1$, $\sigma_k = 1.0$ and $\sigma_\varepsilon = 1.3$.

The justification why the k-ε turbulence model is used

In recent investigations by Khan et al. [1,2,4], the k-ε model was employed to simulate base pressure control in ducts with ribbed geometries at sonic Mach numbers. These studies reported a strong correlation between numerical predictions and experimental measurements of base pressure and related flow parameters, underscoring the model's reliability in internal flow scenarios.

A comparative analysis by Najar et al. [17] specifically evaluated the performance of the k-ε model against other turbulence models, such as the Spalart-Allmaras model, for compressible flow through convergent-divergent nozzles. The study concluded that the k-ε model provided superior predictions of turbulent structures, particularly in capturing the complex interactions within internal flows.

Foundational CFD texts such as those by Tu et al. [23] and Oosthuizen & Carscallen [24] offer a comprehensive overview of turbulence modeling techniques. They highlight the robustness, computational efficiency, and proven track record of the k-ε model in simulating a wide range of internal flow problems. These texts reinforce the practical insights gained from experimental and numerical studies.

The literature consistently demonstrates that the internal flow k-ε turbulence model is well-suited for applications involving sudden expansions and ribbed geometries. Its ability to accurately predict flow separation, reattachment, and associated base pressure dynamics—as evidenced by studies [1,2,4,17], and [25] makes it the optimal choice for our simulations.

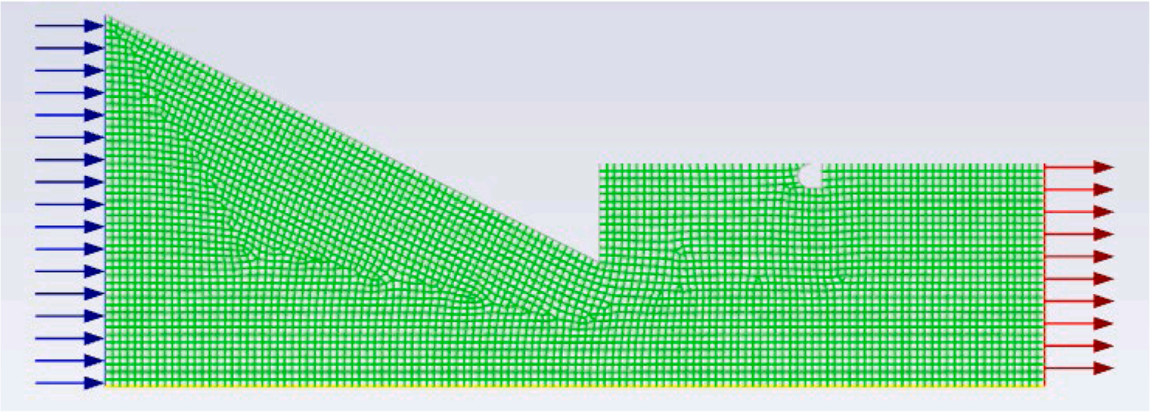

(d)

Fig. 2d. Flow at the inlet and outlet.

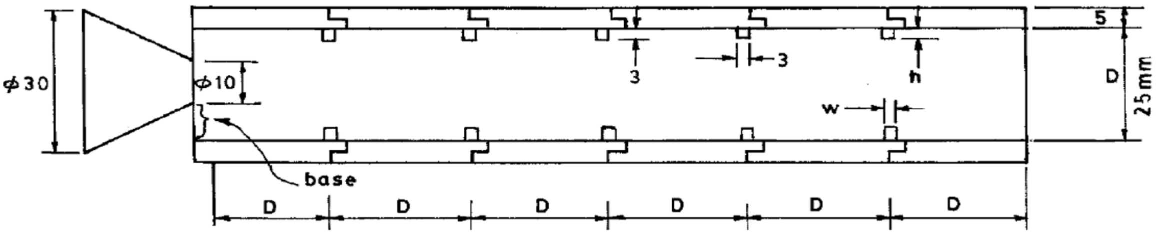

Fig. 3. Duct used in an experimental study by E. Rathakrishnan [25].

5. Finite volume method

5.1. Geometry and modelling

The fluid-flow analyses in this study were conducted using the finite volume method (FVM). The theoretical framework was established through CFD, enabling simulations for a comprehensive parametric study. The simulations were performed using ANSYS Fluent 2024/R2. This study's dimensions and modeling details can be replicated in Fig. 1, and the investigation was carried out in a two-dimensional flow field. Fundamentally, this research can be described as the passive control of high-speed flow through d-shaped ribs using FVM via ANSYS simulations.

5.2. Meshing and boundary conditions

Mesh is a key component of the CFD process. The 2D model is of the structured mesh type since the free-face mesh type was selected. Using the created structured mesh type, elements were sized and built on the dimension of each line (edge). The element dimensions were employed using the lines, and face meshing created elements with the same form. We have completed the mesh independence check. The mesh size and element type that were examined during the mesh independence check are displayed in Fig. 2 below. Mesh independence test for a rib-free, 18 mm duct (L/D = 6). The same geometry model determines the attributes of various element sizes.

Boundary Conditions:

- Pressure Inlet: A pressure inlet boundary condition was applied with the inlet pressure ratio (NPR) of 1.5 to 5 NPR. This range allowed the exploration of different flow regimes under varying pressure conditions.
- No-Slip Wall: All walls, including the surface of the d-shaped rib, were modeled as no-slip walls, ensuring that the fluid velocity at the wall is zero, which is critical for capturing boundary layer development.
- Pressure Outlet: The outlet was set as a gauge pressure outlet under default conditions, ensuring a consistent exit pressure that reflects the experimental environment.

The figure below depicts the fluid dynamics by depicting the directional flow of air inlet and outlet (Fig. 2d).

Boundary Conditions:

- Inlet Conditions:
  - Pressure Inlet: 50,662.5 Pa
  - Total Temperature: 300 K
  - Turbulent Specification: k and epsilon
  - Turbulent Kinetic Energy: 1 m^2/s^2
  - Turbulent Dissipation Rate: 1 m^2/s^3
- Outlet Conditions:
  - Gauge Pressure: 0 Pa
  - Total Temperature: 300 K
  - Backflow Turbulence Model: k-epsilon
  - Backflow Kinetic Energy: 1 m^2/s^2
  - Backflow Dissipation Rate: 1 m^2/s^3
- Wall & Rib Conditions:
  - Material: Aluminum
  - Shear Condition: No-slip
  - Thermal Condition: Heat Flux = 0 W/m^2

Table 1
The geometries of the validation model.

Parameters	Dimensions
The inlet diameter of the nozzle	30 mm
Outlet diameter of the nozzle	10 mm
Tube diameter	25 mm
Tube length	Varies in the range from L/D = 1 to 6
Converging length	20 mm
Rib width	3 mm
Rib height	Varies in the range from 1 mm to 3 mm

5.3. Assumptions and fluid properties

The flow operations are expected to be duplicated in the precise physical environment. The governing equations are simplified by choosing appropriate mathematical and numerical models.

The correct mathematical models must be chosen to solve the governing equations simultaneously, including the governing equations, boundary conditions, mesh quality, and numerical approach. Despite its limitations in accurately modeling physical processes, the computational approach has been used for decades and offers sufficient insight into flow behavior. That means careful consideration must be given to objects resembling the flow behavior. This investigation pinpoints the presumptions that jeopardize the precise physical condition. This study examines the following characteristics and assumptions:

i. The stream is considered a constant 2D flow due to symmetric geometry.
ii. The air's density varies because the flow is compressible. At that Mach number and NPR, the inlet pressure is absolute minus ambient pressure; at the duct's exit, the gauge pressure is zero.
iii. At a particular flow velocity, turbulent flow significantly affects turbulent viscous dissipation; hence, it is considered.
iv. The fluid's temperature affects its viscosity.
v. The flows exit the duct when the air pressure is ambient atmospheric.

The compressible flow field is described by the k-epsilon standard model since the flow through the nozzle is considered turbulent. The following equations are the most suitable for turbulent flow.

5.4. Validation of experimental model

The ANSYS Workbench application uses Fluent methods in computational fluid dynamics (CFD). The model was created using a design modeler. In Fig. 3, a converging nozzle abruptly expands into a duct with five equidistant ribs. According to the experimental setup described by

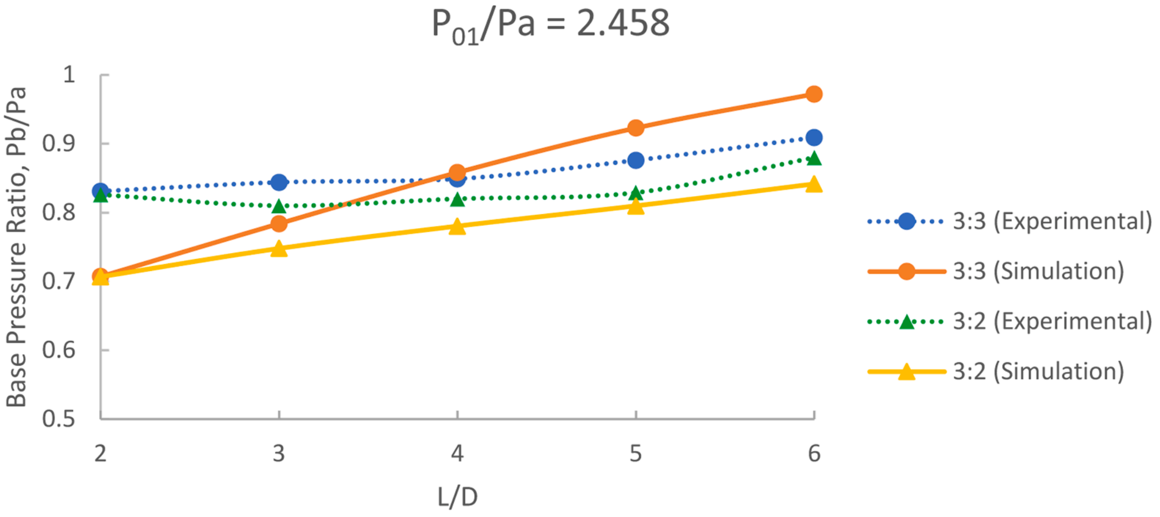

Fig. 4. Validation of CFD results with Experimental results of Rathakrishnan [25].

Table 2
Mesh independence study.

Element size	Coarsest	Coarse	Medium 1	Medium 2	Fine	Finer	Finest
Nodes	2904	3709	9468	25,086	141,004	416,292	2142,592
Elements	2715	3487	10,887	24,594	139,987	414,555	2138,682

Rathakrishnan [25], the converging nozzle's dimensions with an abruptly expanded duct are as follows (Table 1).

The base pressure ratio data curves for the current and previous research are shown in Fig. 3 [25]. Whereas the simulation results produced by ANSYS Fluent were shown as straight lines, the experimental data were shown as dotted lines. Comparing the current numerical analysis to the earlier experimental investigation by Rathakrishnan [25], the percentage difference was less than 10%. As a result, the current work satisfied the acceptance requirements. Each point on the curves was near the next, forming a regular pattern. As a result, the validation of the current work was successful, according to the table and graph previously provided.

The previous study was conducted for width-to-height ratios of 3:1, 3:2, and 3:1; an area ratio of 6.25; L/D ranging from 1 to 6; pressure ratios of 1.141 to 2.458; and nozzle exit Mach numbers of 0.44 to 1.0, according to Rathakrishnan [25]. The CFD results in Fig. 4 for NPR $(P_{01}/P_a) = 2.458$ and ribs of width-to-height ratios 3:2 and 3:3 were used to compare with the experimental results of Rathakrishnan [25]. The experimental work of Rathakrishnan [25], which employed five ribs spaced equally apart in the duct, as seen in Fig. 4, supports the

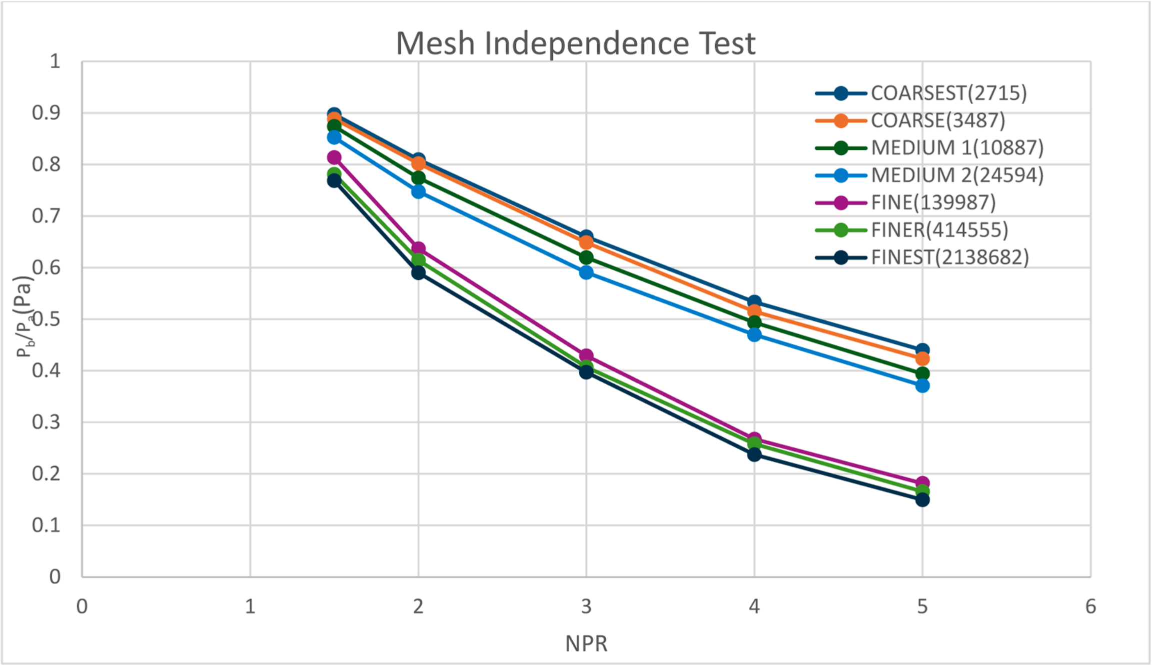

Fig. 5. Results of mesh check.

simulation. L/D varying from 2 to 6 and an NPR of 2.458 are the outcomes of base pressure fluctuation.

5.5. Mesh independence study

Table 2 provides data from a mesh independence study, a crucial step in computational simulations that ensures the results remain consistent regardless of the mesh refinement level.

Each mesh design has a corresponding number of nodes and elements, with element sizes ranging from the coarsest to the finest. There are many more nodes and elements in the finer mesh—1354,262 nodes and 1351,303 elements in the finest mesh compared to 1284 nodes and 1145 elements in the coarsest mesh. This work aims to find the ideal mesh size for precise simulations without needless processing costs. The more the mesh is polished, the more nodes and elements are in the table. With comparatively fewer nodes and elements, the coarsest mesh has a lower computational cost but may be less accurate. On the other hand, the finest mesh requires a large amount of processing power yet provides the highest resolution. The medium and fine meshes balance accuracy and efficiency, offering intermediate granularity levels.

According to the node and element number patterns, the most accurate results will probably come from the finest mesh (Fig. 5). Beyond a certain point, though, mesh refinement may result in diminishing accuracy gains at the expense of a significant increase in computing time. According to a critical evaluation of Table 2, the "Fine" or "Finer" mesh topologies might offer the optimum trade-off between computing efficiency and accuracy. Without approaching the computational cost of the finest mesh, these configurations significantly increase the number of nodes and elements compared to the medium meshes. Further refinement to the finest mesh is not required if simulation results do not differ considerably between the finest and fine meshes. Doing so would increase the computing time without providing additional benefits. Therefore, the best options for more simulation are probably the finer or finer mesh sizes.

6. Results and discussions

Before examining the base pressure data, it is vital to comprehend the physics of the flow when the viscous layer is exhausted to a tube with a more considerable area. The boundary layer will develop and reattach to the duct after being exhausted from the nozzle when the Mach number is less than unity. The divided region will have one or more vortices since the initial vortex is near the base and moderately powerful. The core vortex is the name given to this vortex. Moving fluids from the base region to the main jet on the boundary layer's edge will act as a pump. Low pressure will result from this pushing action in the recirculation zone. Pushing action is excessively erratic because of this vortex spread's known periodicity. The base pressure varies as a result of this erratic pattern. However, tests revealed that these base pressure fluctuations are insignificant. Thus, the data is analyzed using the mean base pressure readings even though most of the time, the base pressure values were the same along the base region. The cyclicity of the vortex shedding may cause the flow pattern of the entire duct to oscillate. These oscillations can become highly severe for specific geometry and inertia values. The area ratio, reattachment section, Mach number, and degree of expansion mainly determine the strength of the primary vortex at the base.

A better understanding of the flow mechanics involved in a larger duct's shear layer exhaustion process would be beneficial before delving into the base pressure discoveries that emerge from the ribs. As the duct exits the nozzle lip, the boundary layer will divide and rejoin when Mach M is less than 1. The initial vortex will be strong and close to the base so that the partitioned area will have one or more vortices. The core vortex is the name given to this vortex. On the border of the shear layer, this pump-like apparatus will move liquids from the base section to the primary jet. This pressing action will cause the recirculation to have low pressure. However, owing to the known cyclical nature of this vortex expansion, the pushing motion is too unpredictable. The result of this erratic pattern will bring changes in the base pressure. The variations in base pressure along the entire base region seem negligible.

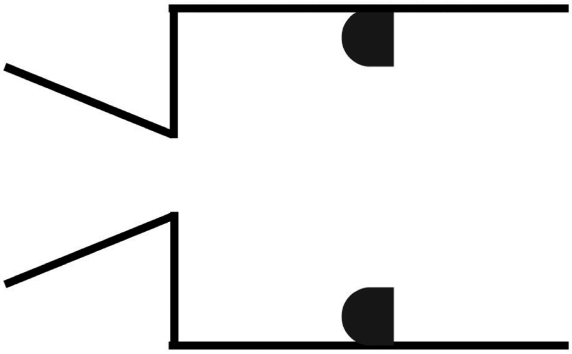

Fig. 6. Converging Nozzle and the duct with d-shape Rib.

However, an average base pressure is considered while analyzing the base pressure data in the current analysis. The vortex cyclicity may cause the extended image's flow pattern to fluctuate. Under specific geometrical and inertia conditions, these oscillations can become extremely severe. The primary factors affecting the core vortex's varying strength at the base are the area ratio, Mach number, reattachment segment, and level of expansion.

This study investigates the effect of d-shaped ribs on the larger duct's base flow and development. When the rib's straight portion faces the base region, orientation one is given a nomenclature. The other side of the ribs is named orientation 2 when the base recirculation region faces the curved surface. Numerical simulations were conducted for both orientations. While performing the simulations, the ribs were oriented in two directions. The first was when the straight side of the rib was towards the base region, and the second was when the curved part faced the base recirculation zone. In addition, the larger duct diameter of 25 mm and the noticeably high area ratio of 6.25 should be mentioned while analyzing the data. When the flow exits the nozzle, it will expand freely and reattach with the enlarged duct to a place different from the ideal one for an intense vortex at the base because of the additional relief provided to the flow.

6.1. Control with orientation 1

Fig. 6 directs the nozzle arrangement with the duct and the passive control as a d-shape rib. The section following the base pressure results for d-shape rib orientation one, when the curved part of the rib faces the base recirculation region, will show later results for orientation two where the straight part of the rib will face flow impinging on the straight part of the d-shape rib. Non-dimensional base pressure results are represented for various rib locations and duct sizes as a function of expansion level.

6.1.1. Pressure contours

The pressure contours presented in the figure demonstrate the effects of a d-shaped control at orientation 1 for high-speed flow in an abruptly expanded duct downstream of a converging nozzle. As the high-speed flow exits the nozzle, it interacts with the d-shaped control, significantly influencing the pressure distribution along the duct. At the 0.5D location (Fig. 7a), a pronounced high-pressure zone appears near the nozzle exit, characterized by red regions. This elevated pressure results from the initial interaction of the sonic jet with the sudden expansion and the obstruction caused by the control device. The flow separates rapidly, creating a recirculation zone, indicated by the blue low-pressure region downstream. This recirculation generates turbulence, increasing energy loss and flow instability.

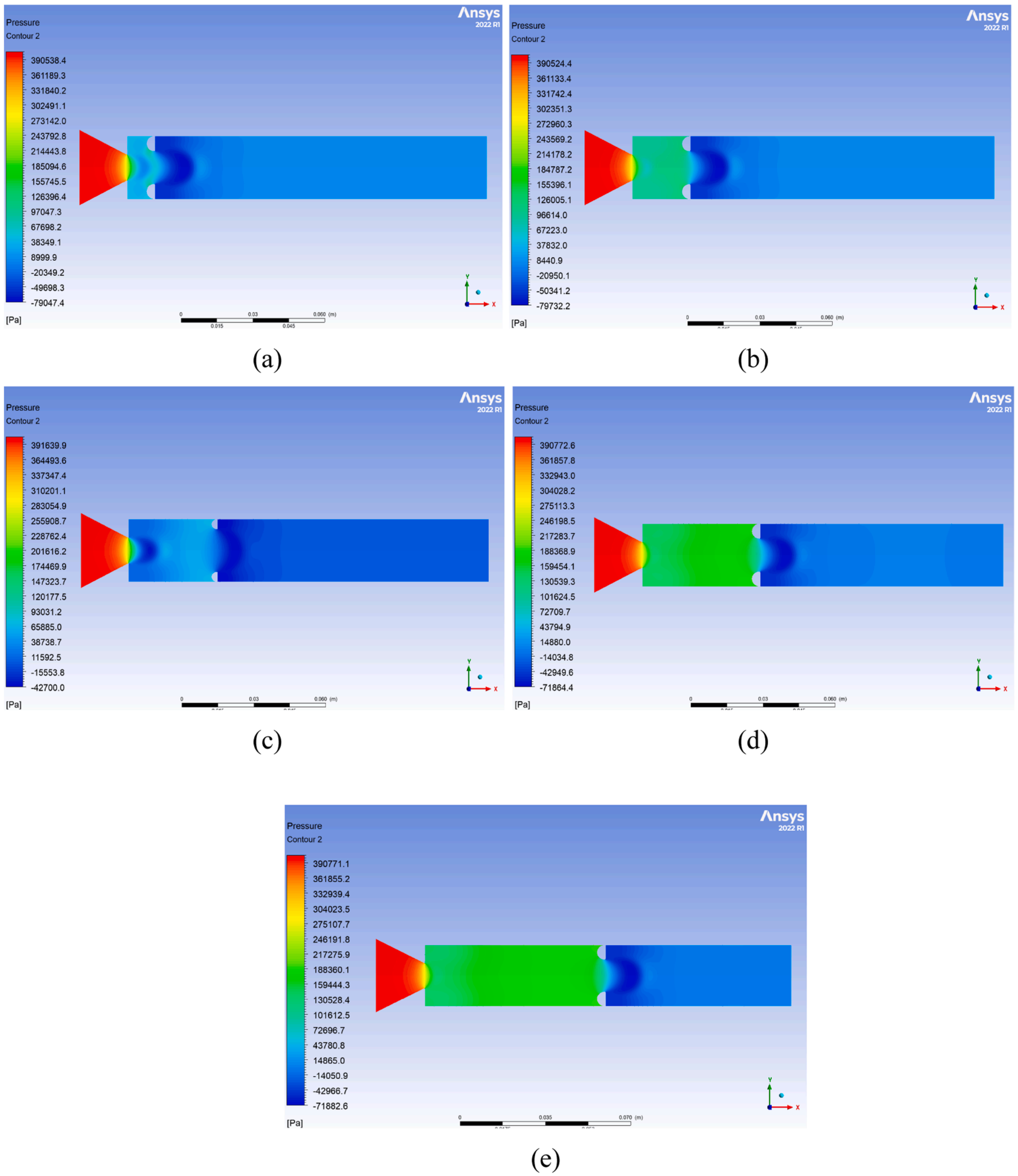

Fig. 7. Pressure contours for 3 mm location at orientation 1 control (a) L/D = 0.5 (b) L/D = 1 (c) L/D = 1.5 (d) L/D = 2.0, and (e) L/D = 3.0.

At the 1.0D location (Fig. 7b), the high-pressure zone immediately after the nozzle exit diminishes, and the pressure distribution becomes more balanced. The recirculation region expands, but the pressure recovers as the flow readjusts to the duct geometry. The green and yellow areas signify a smoother transition from high to low pressure, indicating partial flow stabilization. The flow stabilizes downstream to the 1.5D location (Fig. 7c), with the pressure gradient becoming less steep. The recirculation zone weakens, and the blue low-pressure region shifts downstream, suggesting improved pressure recovery and reduced turbulence intensity.

The pressure contours show further stabilization at the L/D = 2.0 location (Fig. 7d), significantly reducing the high-pressure zone about the nozzle exit. The flow becomes more streamlined, and the recirculation zone continues to shrink. The pressure recovery is more uniform, as evidenced by the broader green region. Finally, the flow achieves near-complete stabilization at the L/D = 3.0 location (Fig. 7e). The high-pressure zone close to the nozzle exit almost disappears, and the pressure distribution across the duct becomes uniform. The recirculation zone is minimal, indicating efficient pressure recovery and reduced energy loss. The pressure contours reveal that the d-shaped control modifies the flow field, initially causing significant separation and turbulence near the nozzle exit. However, as the flow progresses downstream, pressure recovery improves, and the flow becomes more uniform. This suggests that while the control device induces initial flow

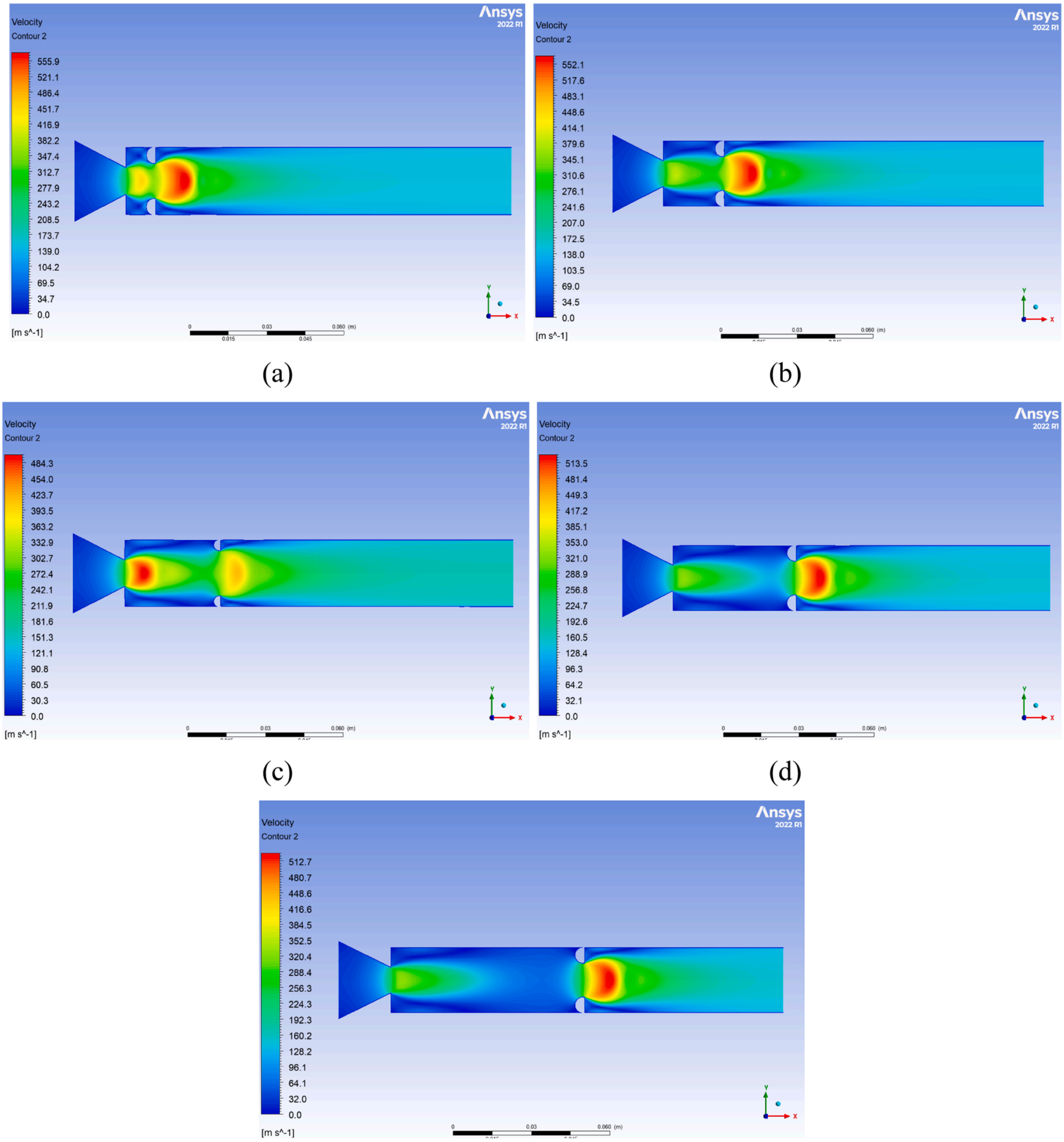

(a) (b)

(c) (d)

(e)

Fig. 8. Velocity contours for 3 mm location at orientation 1 control (a) L/D = 0.5 (b) L/D = 1.0 (c) L/D = 1.5 (d) L/D = 2.0 (e) L/D = 3.

disturbances, it ultimately enhances flow stability and pressure distribution along the duct, which is crucial for efficient high-speed flow management in suddenly expanded ducts.

6.1.2. Velocity contours

The velocity contours presented in the diagram demonstrate the effects of the d-shaped control at orientation 1 for high-speed flow in a rapidly expanded duct downstream of a convergent nozzle. These contours highlight the velocity distribution at five locations from the nozzle exit: (a) L/D = 0.5, (b) L/D = 1, (c) L/D = 1.5, (d) L/D = 2.0, and (e) L/D = 3.0, where L/D represents the duct length-to-diameter ratio. The figure’s color gradient represents the velocity magnitude, with red implying high-velocity zones and blue representing low-velocity zones. Analyzing these velocity contours provides insights into how the d-shaped control influences flow acceleration, deceleration, and recirculation across the duct.

At the 0.5D location (Fig. 8a), the velocity contour shows a significant high-velocity jet exiting the CD nozzle, indicated by the red zone. The presence of the d-shaped control disrupts the flow, causing a rapid expansion and subsequent flow separation. The low-velocity region (blue zone) immediately downstream of the control device indicates the setup of a recirculation region. This zone results from the adverse pressure gradient created by sudden expansion, leading to significant energy loss and flow instability. For the rib location at 1.0D (Fig. 8b), the high-velocity core continues to dominate the central axis of the duct, but the recirculation zone downstream of the control device expands. The velocity gradient becomes more pronounced, with the high-speed jet gradually mixing with the surrounding low-speed flow—the

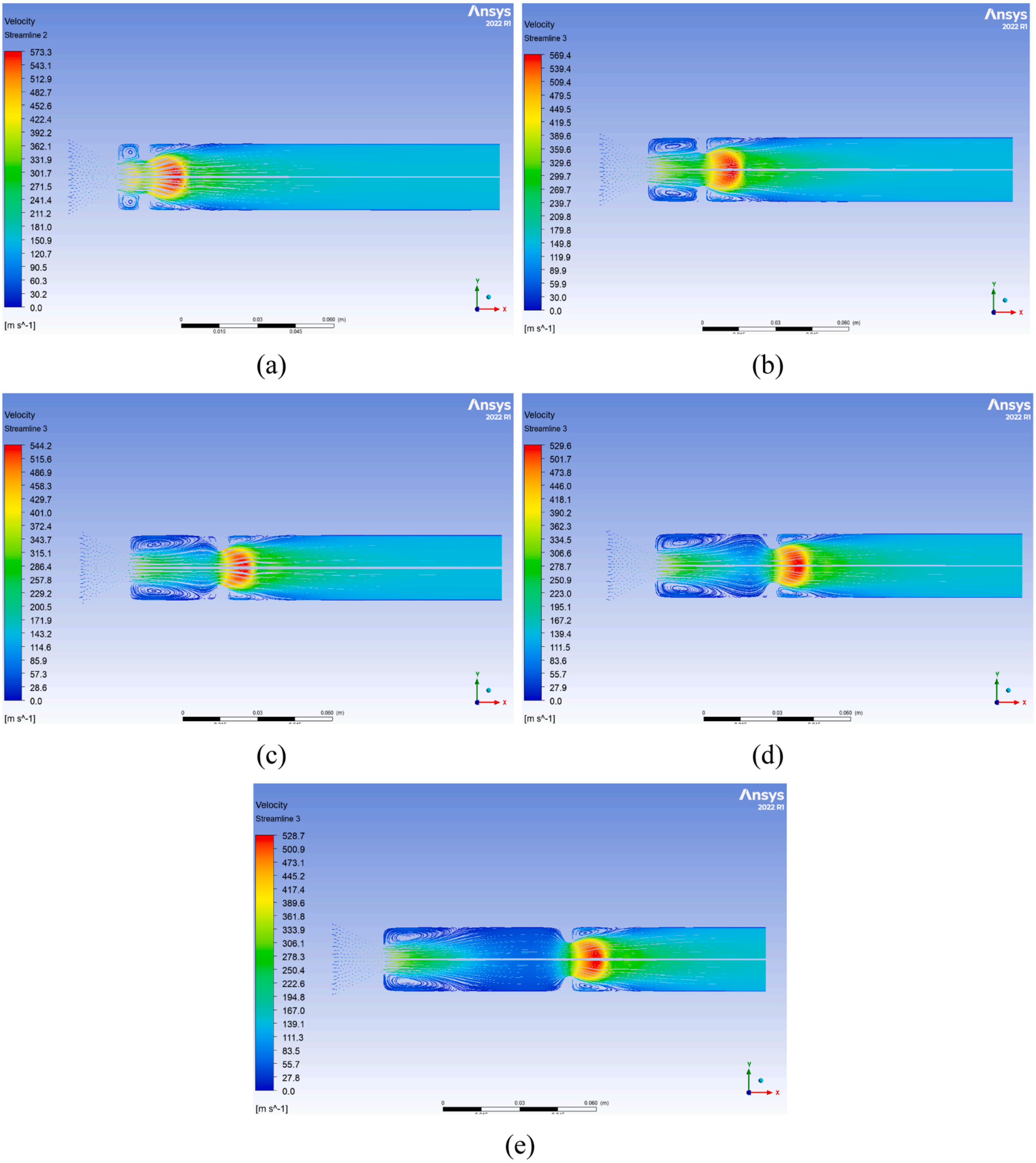

Fig. 9. Streamline contours for 3 mm location at orientation 1 control (a) L/D = 0.5 (b) L/D = 1.0 (c) L/D = 1.5 (d) L/D = 2.0 (e) L/D = 3.

collaboration between the main jet and the recirculating stream results in increased turbulence and flow instability. At the 1.5D location (Fig. 8c), the velocity distribution shows partial recovery, with the high-velocity core becoming more streamlined. The recirculation zone weakens, and the low-velocity region near the duct walls shrinks. The transition from red to green and blue areas indicates the flow stabilizes, with reduced turbulence and improved velocity uniformity across the duct. The velocity contours in the 2.0D location (Fig. 8d) reveal further flow stabilization. The high-velocity jet continues to dominate the center of the duct, but the surrounding low-speed regions become more uniform. The recirculation zone diminishes, and the velocity distribution becomes more balanced, suggesting improved flow recovery and reduced energy loss.

Lastly, the velocity contours demonstrate near-complete flow stabilization at the 3.0D location (Fig. 8e). The high-velocity core remains well-defined, but the surrounding flow achieves a more uniform distribution. The recirculation zone is minimal, indicating efficient mixing and energy recovery. The flow at this stage is well-organized, with reduced turbulence and improved overall velocity uniformity across the duct. Overall, the velocity contours for orientation one control demonstrate that the d-shaped control initially induces significant flow separation and turbulence near the nozzle exit. However, velocity recovery improves as the flow progresses downstream, the recirculation zone shrinks, and the flow stabilizes. This suggests that while the control device initially disrupts the flow, it ultimately enhances flow uniformity and efficiency along the duct.

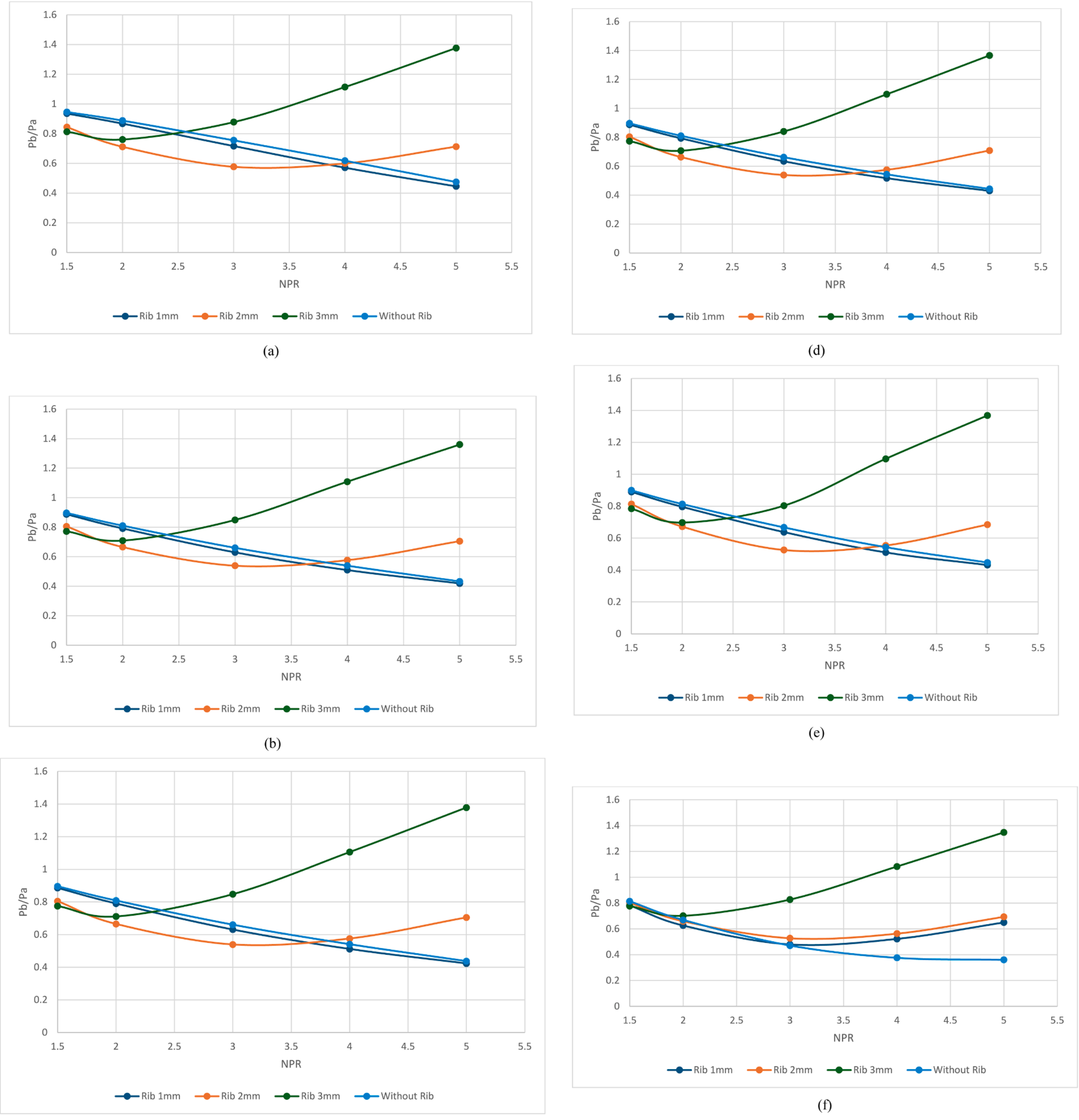

(a)

(b)

(c)

(d)

(e)

(f)

Fig. 10. Base Pressure Vs. NPR for numerous tube sizes.

6.1.3. *Streamline formation contours*

The streamline contours for orientation one control illustrate the flow behavior and streamline formation as the high-speed flow exits the convergent nozzle and expands into the abruptly expanded duct. The streamlines reveal the stream patterns, including recirculation zones, flow separation, and reattachment points, across five downstream locations: (a) L/D = 0.5 (b) L/D = 1 (c) L/D = 1.5 (d) L/D = 2.0 and (e) L/D = 3.0, where D represents the duct diameter. These streamline formations provide insight into how the d-shaped control affects the flow dynamics in the duct.

At the 0.5D location (Fig. 9a), the streamline contours show a significant disturbance in the flow immediately downstream of the nozzle exit. The high-speed jet exiting the nozzle interacts with the d-shaped control, causing flow separation and the formation of a strong recirculation zone on both sides of the control device. This recirculation is characterized by swirling streamlines, indicating the presence of vortices due to the sudden expansion and the obstruction created by the control. The central core of the flow remains streamlined, but the surrounding flow exhibits chaotic behavior, leading to increased turbulence and energy loss. At the 1.0D location (Fig. 9b), the recirculation zone expands further downstream, with the streamlines continuing to exhibit swirling patterns near the duct walls. The high-speed jet maintains its core structure along the duct centerline while the flow near the walls remains disturbed. The streamlines show the formation of secondary vortices, indicating ongoing flow instability and incomplete pressure recovery at this stage. The communication involving the high-speed jet and the recirculating flow further enhances mixing but increases flow resistance. Streamlining patterns reveal partial flow stabilization by the 1.5D location (Fig. 9c). The central core of the flow becomes more organized, with fewer disturbances along the centerline. However, the recirculation zones near the duct walls persist, though their intensity decreases compared to upstream locations. The streamlines align more uniformly, indicating that the flow is gradually adapting to the expanded duct geometry and the presence of the d-shaped control. At

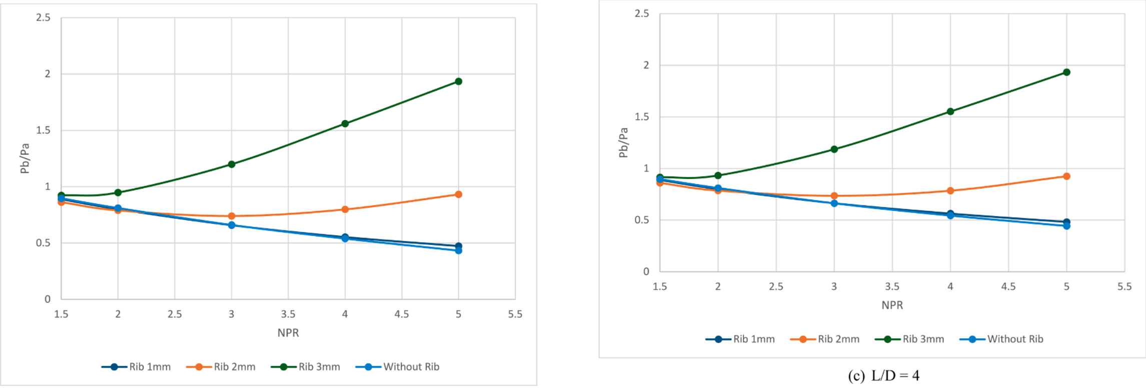

(a) L/D = 2

(c) L/D = 4

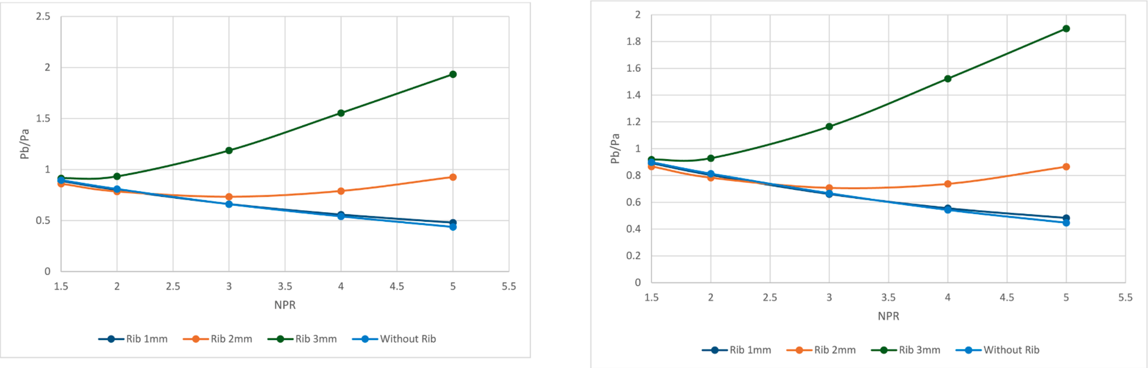

(b) L/D = 3

(d) L/D = 5

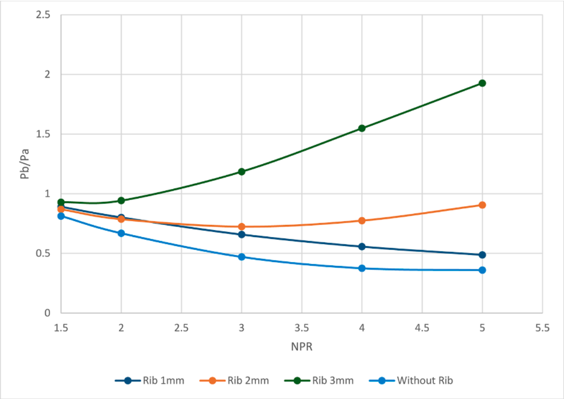

(e) L/D = 6

Fig. 11. Base Pressure Vs. NPR for numerous duct sizes.

the 2.0D location (Fig. 9d), the streamline contours exhibit further stabilization, with the recirculation zones diminishing in size and intensity. The high-speed jet along the centerline remains well-defined, while the surrounding flow achieves a more streamlined structure. The formation of vortices reduces, indicating improved pressure recovery and reduced energy loss. The flow near the duct walls becomes more organized, suggesting that the influence of the d-shaped control is gradually diminishing downstream.

Ultimately, the streamline contours demonstrate near-complete flow stabilization at the 3.0D location (Fig. 9e). The central high-speed jet remains intact, with the surrounding flow achieving a more uniform distribution. The recirculation zones are minimal, and the streamlines align more closely with the duct walls, indicating efficient flow recovery and reduced turbulence. The flow at this stage is well-organized and less chaotic, suggesting that the control's impact has been effectively integrated into the overall flow structure. Overall, the streamline contours for orientation one control reveal that while the d-shaped control initially induces significant flow separation and turbulence about the nozzle outlet, the flow gradually stabilizes as it progresses downstream. The recirculation zones shrink, the flow becomes more streamlined, and the overall aerodynamic efficiency improves, indicating the effective role of the control device in managing high-speed flow expansion in the duct.

6.1.4. *Base pressure results when rib is located at L/D = 0.5*

The base pressure findings at various expansion levels for duct L/D ratios ranging from 1 to 6 are shown in Fig. 10((a) to (f)) when the passive control is set at L/D = 0.5. Centered on the findings, it is evident that the base pressure for each NPR is trending downward. The stream from the converging nozzle liquidated into the expanded duct may connect with a reattachment distance different than the ideal for a strong vortex at the base when the relief effect caused by the increase in the area ratio exceeds a certain threshold. Because of this mechanism, the impact of NPR on base pressure becomes negligible at larger area

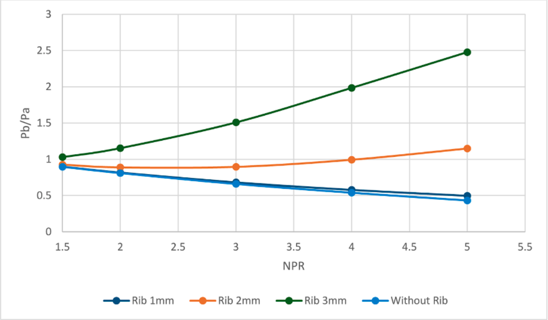

(a) L/D = 2

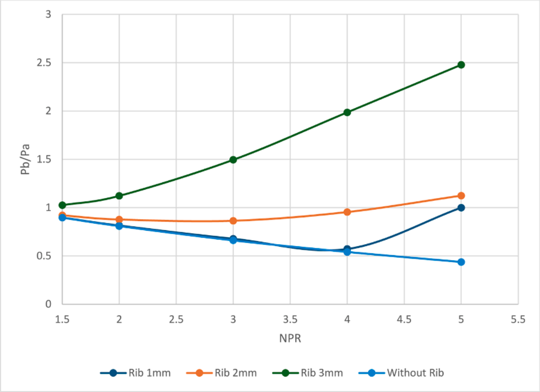

(b) L/D = 3

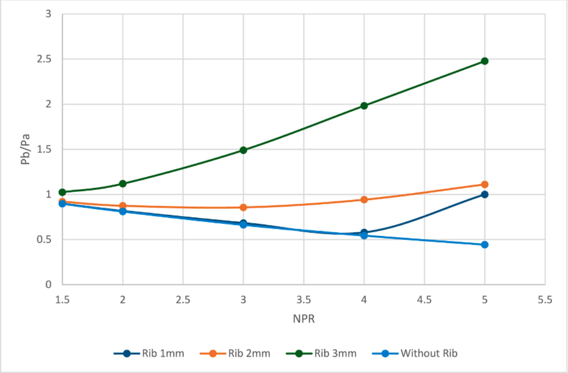

(c) L/D = 4

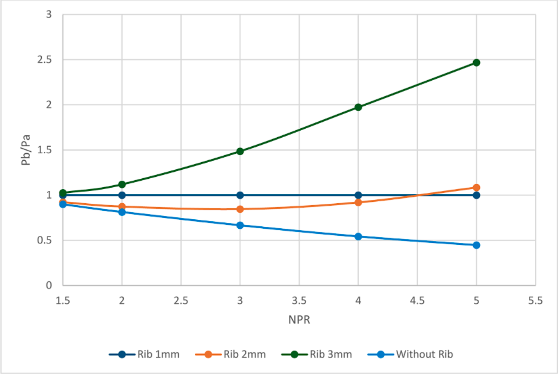

(d) L/D = 5

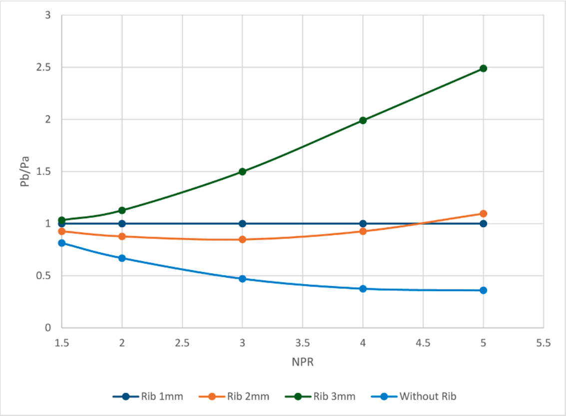

(e) L/D = 6

Fig. 12. Base Pressure Vs. NPR for numerous duct sizes.

ratios.

It is observed that the passive control with a d-shaped rib causes the base pressure to decrease for all of the NPRs in the current study once the stream from the converging nozzle is choked. However, when rib 2 mm is used to control the base pressure up to NPR = 3, the base pressure continues to decrease; however, from NPR greater than three, there is a slight increase in the base pressure, and its maximum value is 30% lesser than the freestream pressure (Fig. 10(a)).

The base pressure consequences gradually rise once the nozzle is choked when we examine the base pressure caused by a 3 mm rib height. The nozzle flow must cross the advantageous pressure gradient (i.e., under-expanded nozzle) for the control to be successful. The base pressure value for NPR = 5 is 40% higher than the ambient pressure. The flow is still growing in the expanded duct for this rib site. Because the location of the ribs is near the base recirculation region, we cannot remark on the findings. Because secondary vortices cannot have any effect, there is a slight rise in base pressure at rib heights of 2 mm at large NPRs. Therefore, we may conclude that passive control is insufficient for 1 mm and 2 mm rib heights. Other duct lengths, specifically L/D = 2, 3, 4, 5, and 6, show similar results, with slight differences brought on by variations in the L/D Ratio and the impact of back pressure.

6.1.5. *Base pressure results when rib is located at L/D = 1*

When the rib is located at L/D = 1, the base pressure findings are shown in Fig. 11((a) to (e)) for NPRs in the range from 1.5 to 5 and for L/D ratios in the range from 1 to 6. For duct L/D = 2, the results are presented in Fig. 11(a), and the figure shows that a 1 mm rib is ineffective. It may be due to the higher inertia level of the primary jet. Once the flow gets separated, there is little interaction between the secondary vortices produced by the rib, the dividing streamlines, and the primary vortex positioned in the base region. Again, the boundary layer will be formed during this process, blocking the flow towards the base region.

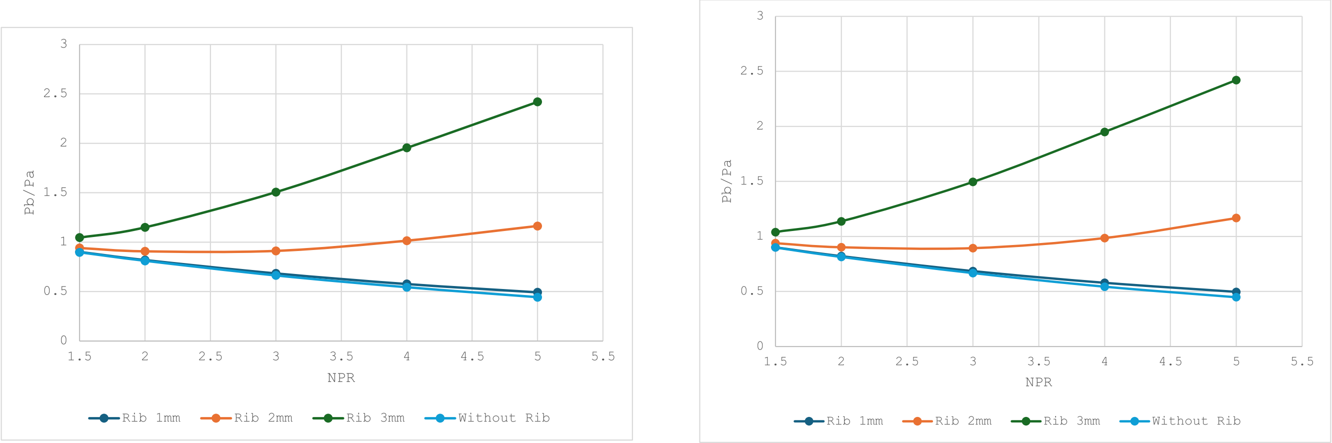

(a) L/D = 3

(b) L/D = 4

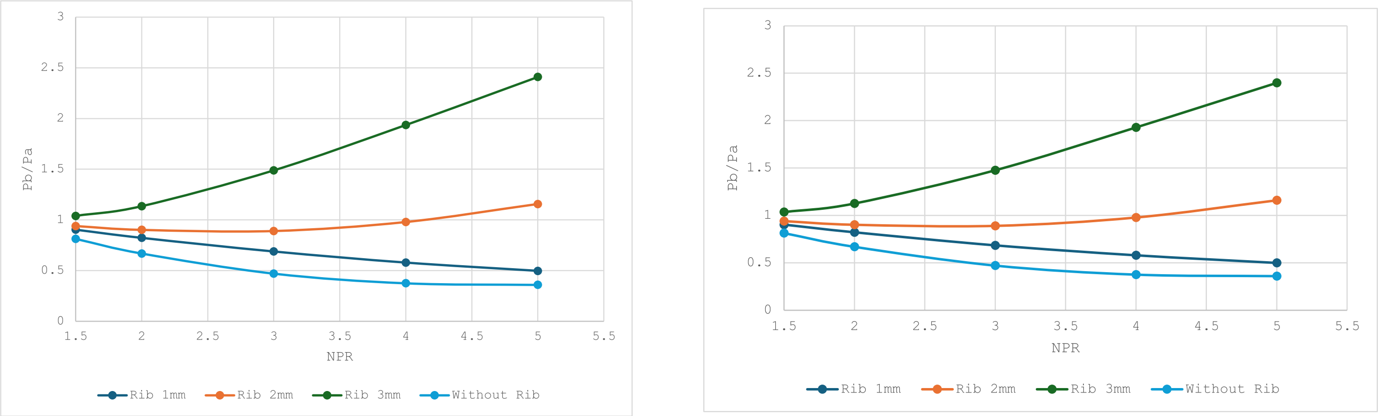

(c) L/D = 5

(d) L/D = 6

Fig. 13. Base Pressure Vs. NPR for numerous ducts.

For rib height 2 mm, once the flow is choked, the downward trend of the base pressure gets halted, and at the highest value of the NPR, the base pressure accomplishes a value very close to the back pressure. When we see the results for the 3 mm height of the rib, it is seen that right from the NPR = 1.5, there is a growing trend in the base pressure, and at NPR = 5, the base pressure ratio is nearly two. This rise in the base pressure is attributable to the more considerable rib height, strong vortices, and backflow towards the base region.

Analogous results are obtained for other duct segments, namely L/D = 3, 4, and 5, as observed for L/D = 2. Base Pressure results for L/D = 6 are displayed in Fig. 11(e), and these results are entirely different from lower duct lengths, namely L/D = 2 to 5, where the rib with 1 mm height was inefficient, and the base pressure with and without control is nearly the same. For this particular duct size, control is effective for all the values of NPRs, and control results in a 30 % increase in the base pressure. This pattern in the base pressure values may be ascribed to the considerable duct length and the freestream pressure being unable to influence the control effectiveness of the rib, as the reattachment location might be L/D = 3 to 4. Hence, this pattern is expected.

6.1.6. *Base pressure results when rib is located at L/D = 1.5*

The base pressure results for different duct sizes and NPRs in the current investigation are displayed in Fig. 12((a) to (e)) when the rib was positioned at L/D = 1.5. As shown in Fig. 12(a), with L/D = 1, the control efficiency of 1 mm and 2 mm is the same. However, the base pressure ratio reached 2.5 for a 3 mm rib (Fig. 12(a)). In contrast to earlier occurrences, this might be because the rib site is now closed to reattachment. When the (L/D) = 3D, the base pressure values for the 1 mm rib fluctuate significantly. This was ineffective when the under-expansion intensity was high, and the base pressure ratio values equaled the ambient pressure. The base pressure ratio for this flow and geometric parameters equals unity (Fig. 12(b)). The basal pressure values for 2-mm and 3-mm rib heights remain unchanged. Fig. 12(c) shows similar results for L/D = 4. The base pressure results for 3 mm rib show no change when we examine the data for L/D = 5 and 6; for 1 mm rib, the base pressure is independent of NPR. However, for 2 mm ribs, the tendency is downward until NPR = 4.5; beyond that, the base pressure rises for NPRs larger than 4.5. Although the nozzle is flowing under the effect of the encouraging pressure gradient, these outcomes confirm that the control is insufficient when the area of the enlarged duct exceeds a specific range (Fig. 12(d) to (e)).

6.1.7. *Base pressure results when rib is located at L/D = 2*

For NPRs in the extent of 1.5 to 5 for duct segment L = 3D to 6D, Fig. 13((a) to (d)) displays the base pressure results for rib position at L/D = 2. A 1 mm rib cannot significantly alter the duct's flow field, as shown in Fig. 13(a). The base pressure, with and without control, is almost constant, except for a slight variation at NPRs 4 to 5. The base pressure ratio for 2 mm and 3 mm ribs stayed at 1.2 and 2.45, respectively, as determined for rib position L/D = 1.5. The reattachment location will be at L/D = 3 and 4, and backpressure will affect the flow within the duct, according to the flow's mechanics.

The results of this study for 1 mm rib differ for both duct sizes when we examine the data for L/D = 5 and 6. The base pressure ratios for 1 mm ribs have changed significantly; the declining trends in the base pressure have been reviewed even though the base pressure ratios for 2 mm and 3 mm ribs remain unchanged. In contrast to those without rib cases, base pressure ratios are higher for 1 mm ribs. The unusual base

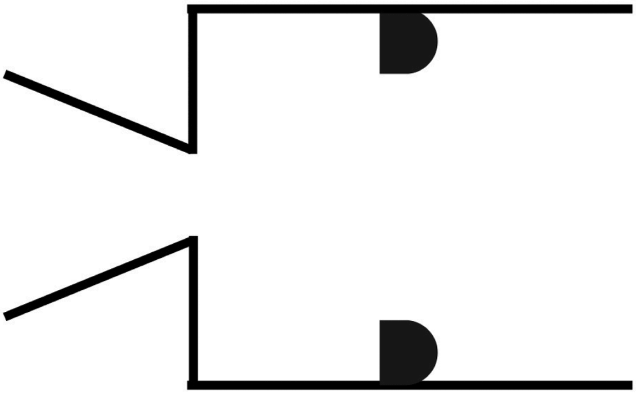

Fig. 14. Converging Nozzle and Duct with d-shape Rib.

pressure ratio behavior can be attributed to the duct length, which is quite significant. Suction is produced again in these conditions, although it was not present for lower duct lengths, specifically L/D = 3 and 4.

6.2. *Control with rib orientation 2*

Fig. 14 shows the orientation of the rib as 2. In this arrangement, the flat part of the rib faces the base region, and the curved part is downstream or at the aft of the rib. In the previous case, as displayed in Fig. 6, the curved part of the rib faces the base region, and the vertically flat part is downstream. In this study, the ribs were kept at two different orientations to ascertain the effectiveness of the ribs in both cases.

6.2.1. *Pressure contours*

The pressure contours in the figure depict the effects of the d-shaped control at orientation 2 for high-speed flow through an abruptly

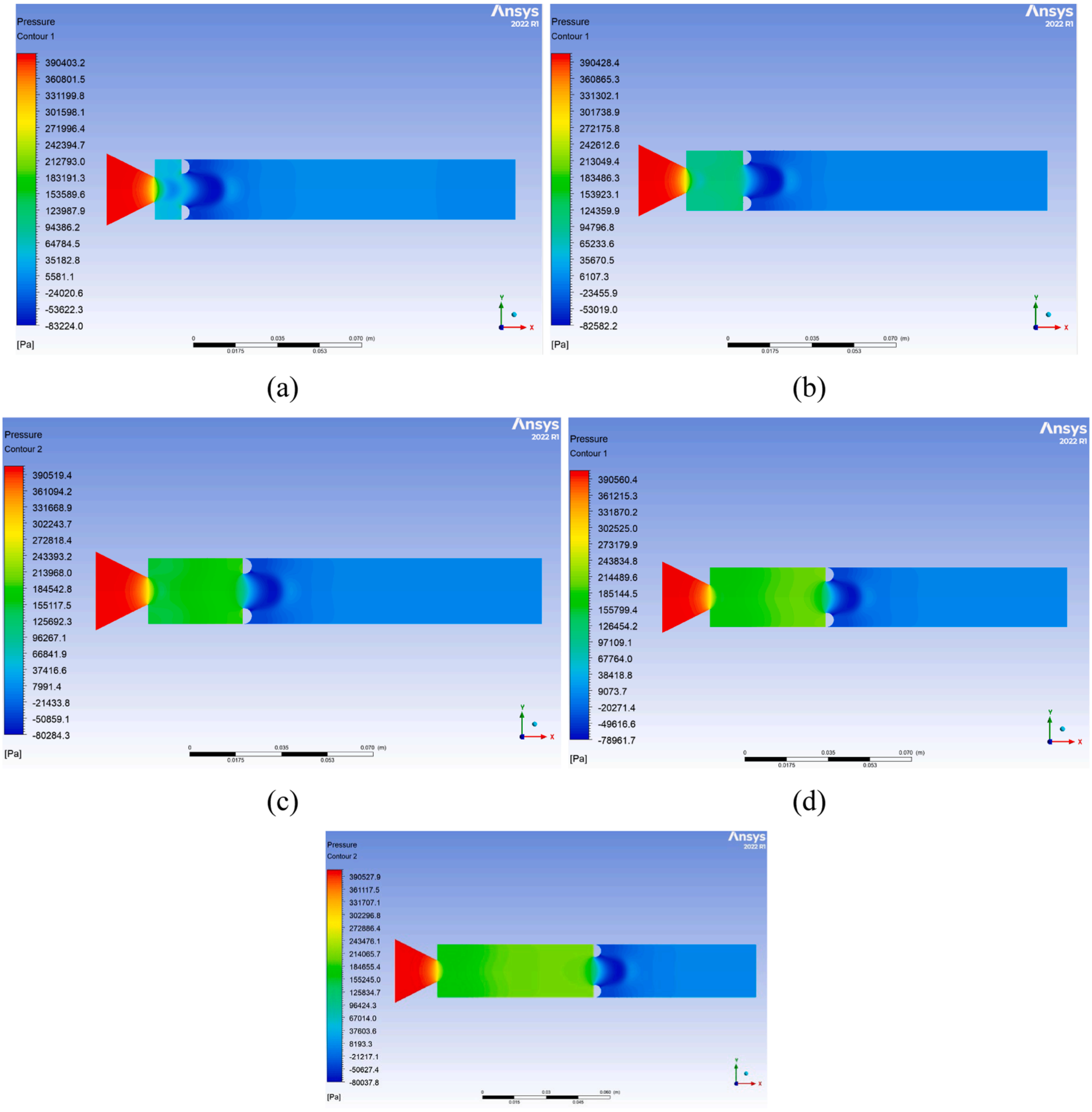

(a) (b) (c) (d) (e)

Fig. 15. Pressure contours for 3 mm location at orientation two control (a) L/D = 0.5 (b) L/D = 1 (c) L/D = 1.5 (d) L/D = 2.0 and (e) L/D = 3.0.

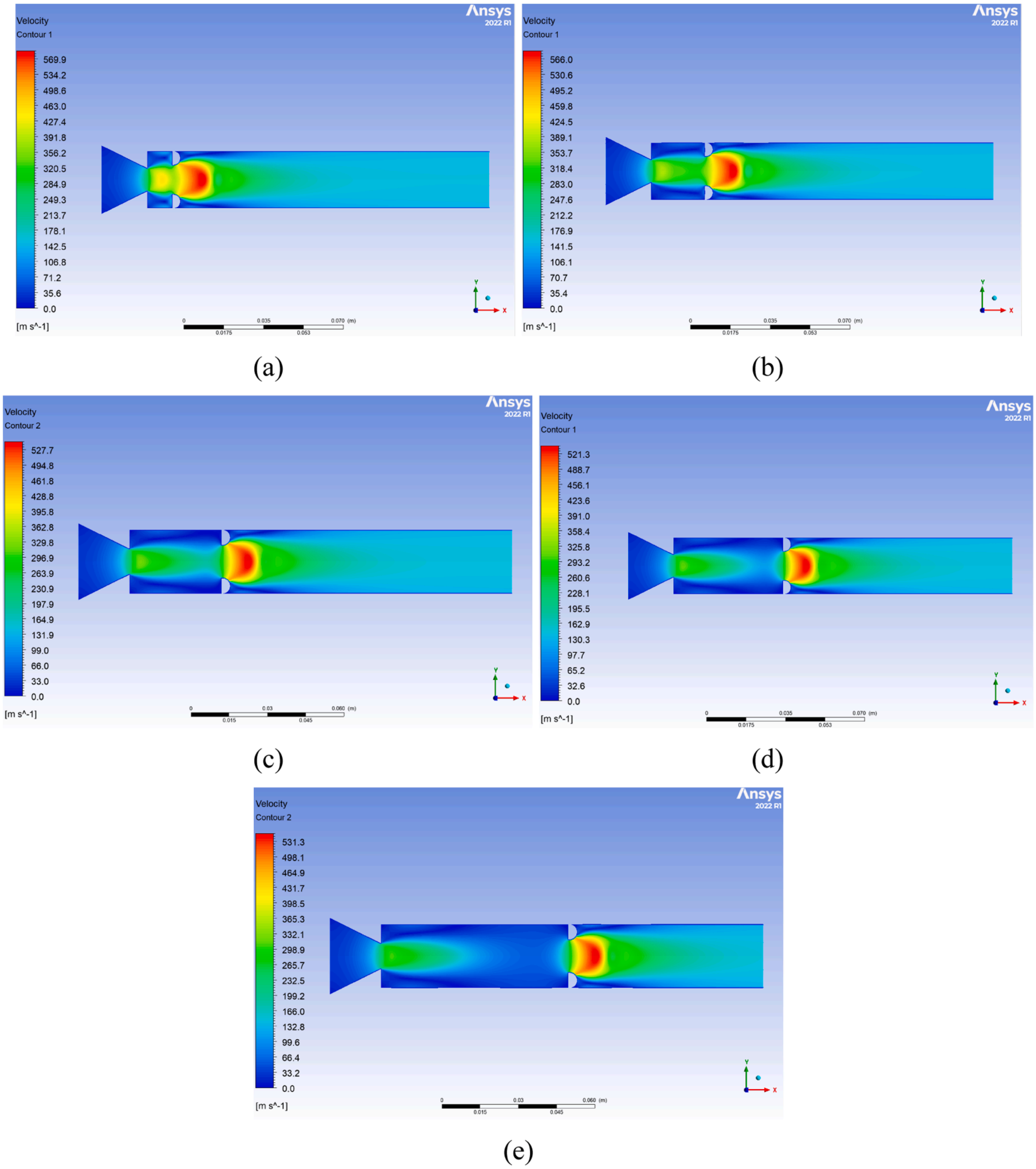

Fig. 16. Velocity contours for 3 mm location at orientation 2 control (a) L/D = 0.5 (b) L/D = 1.0 (c) L/D = 1.5 (d) L/D = 2.0 (e) L/D = 3.

expanded duct connected to a convergent nozzle. The figure showcases the pressure distribution at five downstream locations from the nozzle exit: L/Ds = 0.5, 1.0, 1.5, 2.0, and 3.0, where L/D represents the slenderness ratio of the tube. The color gradient shows the pressure disparities, with red indicating high-pressure zones and blue signifying low-pressure zones. These contours provide a detailed understanding of how the orientation two control influences flow separation, pressure recovery, and overall flow stability within the duct.

At the L/D = 0.5 location (Fig. 15a), the pressure contour reveals a prominent high-pressure zone adjacent to the nozzle exit, as denoted by the red region. This elevated pressure results from the interaction between the high-speed jet exiting the CD nozzle and the d-shaped control, obstructing the expansion and creating a strong recirculation zone. The low-pressure region (blue area) downstream signifies significant flow separation and turbulence, leading to energy loss and instability in the flow field. In the 1.0D location (Fig. 15b), the high-pressure zone close to the nozzle exit reduces, and the pressure gradient becomes more evenly distributed along the duct. The recirculation zone downstream expands while the pressure recovers as the flow readjusts to the new duct geometry. The transition from red to green and blue regions indicates partial flow stabilization, with turbulence persisting near the control device. At the 1.5D location (Fig. 15c), the pressure distribution shows further improvement, with the high-pressure zone near the nozzle exit continuing to diminish. The recirculation zone weakens, and the pressure gradient becomes less steep. More uniform green and light blue regions indicate that the flow stabilizes, with reduced turbulence and better pressure recovery along the duct length. The pressure contours exhibit further stabilization in the 2.0D location (Fig. 15d). The high-pressure zone near the nozzle exit becomes less pronounced, and the flow downstream becomes more streamlined. The recirculation zone continues to shrink, and the pressure recovery improves, as evidenced by the broader green region extending along the duct. That suggests that

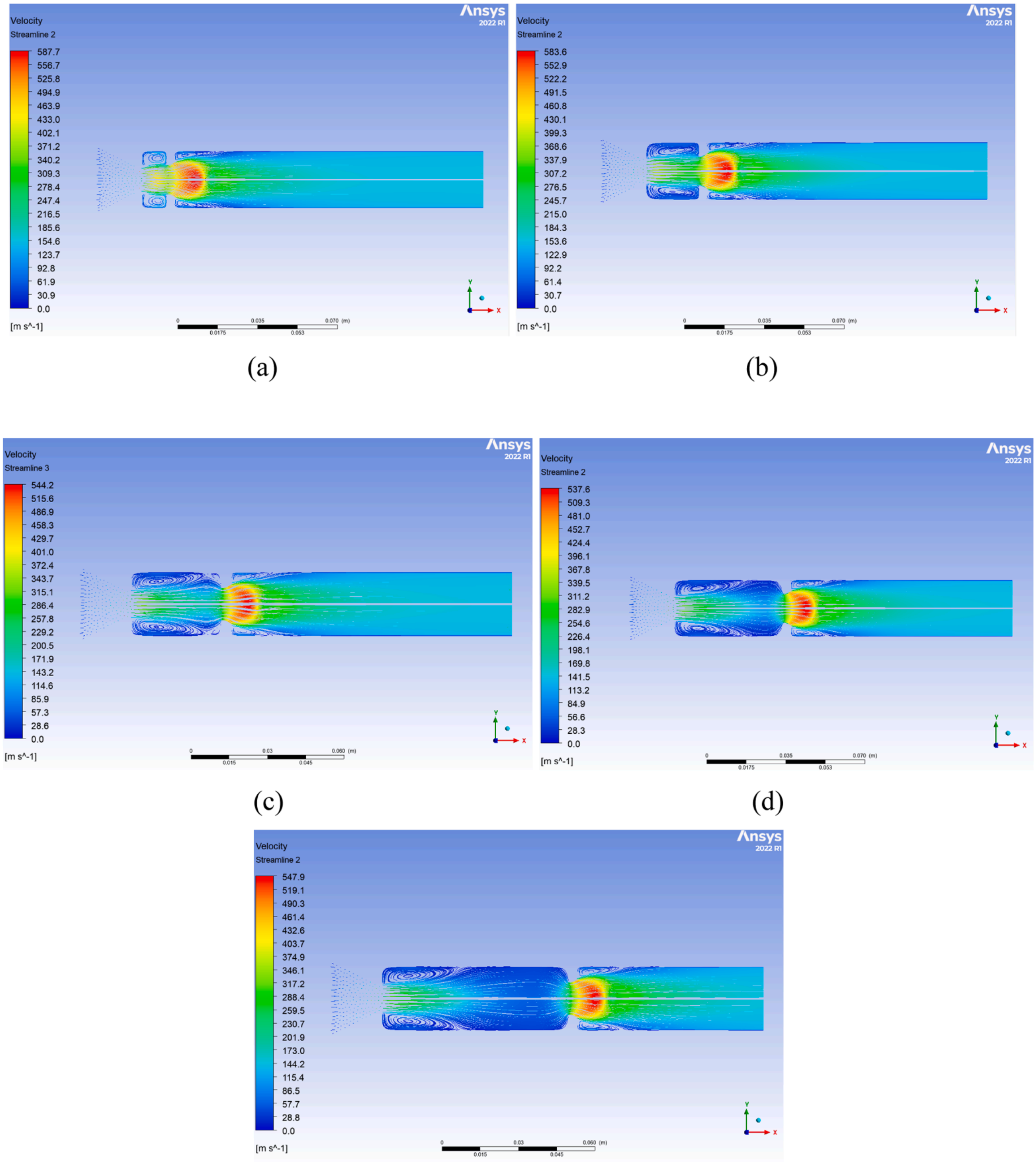

(a) (b)

(c) (d)

(e)

Fig. 17. Streamline contours for 3 mm location at orientation 2 control (a) L/D = 0.5 (b) L/D = 1.0 (c) L/D = 1.5 (d) L/D = 2.0 (e) L/D = 3.

the influence of the d-shaped control is gradually diminishing, allowing for more efficient flow management.

Finally, the pressure distribution achieves near-complete stabilization at the 3.0D location (Fig. 15e). The high-pressure zone close to the nozzle exit disappears, and the pressure gradient across the duct becomes uniform. The recirculation zone behind the control device is minimal, indicating efficient pressure recovery and reduced energy loss. The flow at this stage is well-organized and less turbulent, suggesting that the control's impact has been effectively integrated into the overall flow structure. Overall, the pressure contours for orientation two control demonstrate that the d-shaped control initially induces significant flow separation and turbulence about the nozzle exit. However, as the flow progresses downstream, pressure recovery improves, the recirculation zone shrinks, and the flow stabilizes. That indicates that orientation two control effectively manages high-speed flow expansion in a suddenly expanded duct, enhancing overall aerodynamic performance.

6.2.2. *Velocity contours*

The velocity curves for the orientation two control illustrate the effects of the d-shaped control on high-speed flow through the duct downstream of a convergent nozzle. These contours are presented for five downstream locations from the nozzle exit: L/D = 0.5, 1.0, 1.5, 2.0, and 3.0, where L/D is the length-to-diameter ratio of the tube. The color gradient signifies the velocity magnitude, with red indicating high-speed regions and blue denoting low-speed zones. The analysis of these contours provides insight into the flow characteristics, including velocity gradients, flow separation, and recirculation patterns induced by the d-shaped control.

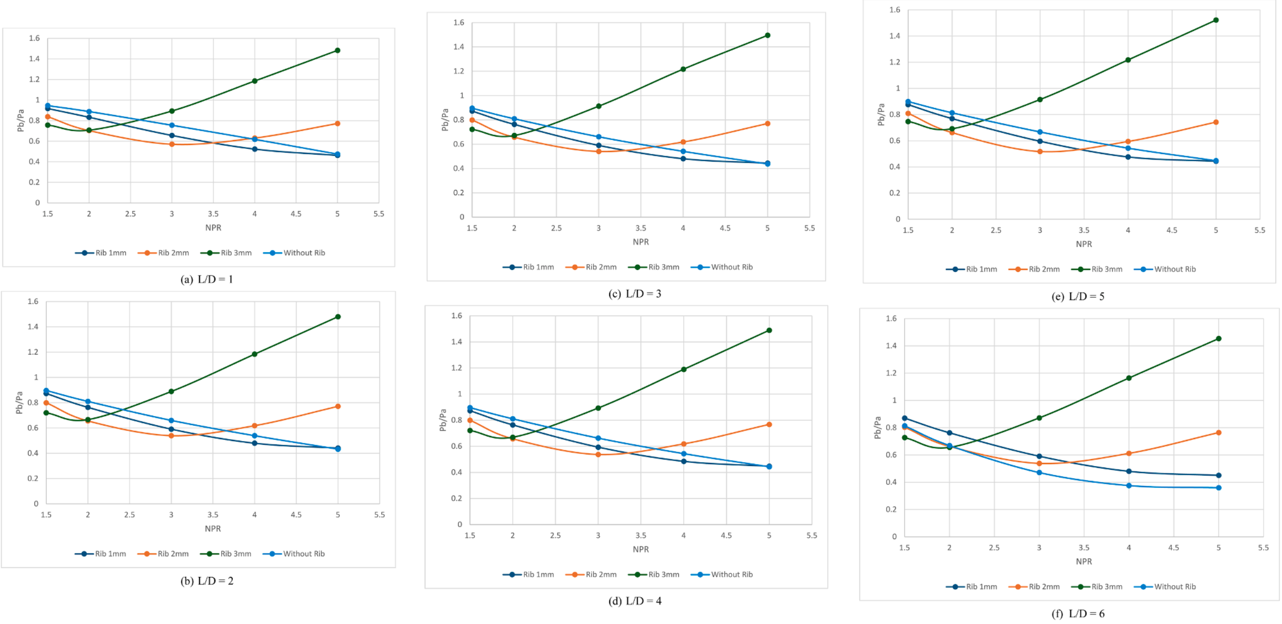

(a) L/D = 1

(b) L/D = 2

(c) L/D = 3

(d) L/D = 4

(e) L/D = 5

(f) L/D = 6

Fig. 18. Base Pressure Variation with NPR for various duct lengths.

At the 0.5D location (Fig. 16a), the velocity contours reveal a high-speed jet exiting the nozzle, represented by the red zone along the central axis. The interaction between the high-speed jet and the d-shaped control induces a strong recirculation zone downstream, evidenced by the surrounding low-velocity blue region. The sudden expansion causes the flow to separate, leading to significant turbulence and energy loss. This recirculation results in poor flow recovery and non-uniform velocity distribution across the duct. At the 1.0D location (Fig. 16b), the high-velocity core continues to dominate the flow along the duct's centerline, but the recirculation zone expands further downstream. The velocity gradient becomes more prominent, with the high-speed jet interacting more extensively with the low-speed recirculating flow near the duct walls. This interaction increases turbulence intensity and enhances mixing between the core jet and the surrounding flow.

The velocity contours indicate partial flow recovery by the 1.5D location (Fig. 16c). The high-speed core remains prominent but becomes more streamlined while the recirculation zone weakens. The transition from red to green and blue regions suggests a more balanced velocity distribution, with reduced turbulence and more stable flow conditions. The velocity gradient near the walls decreases, indicating improved mixing and flow uniformity across the duct cross-section. The flow shows significant stabilization at the 2.0D location (Fig. 16d). The high-velocity jet remains confined to the centerline, while the surrounding low-speed regions become more uniform. The recirculation zone continues to shrink, and the velocity distribution appears more balanced. The reduction in flow separation suggests that the influence of the d-shaped control weakens as the flow progresses downstream, leading to improved pressure recovery and reduced energy loss.

Ultimately, the velocity contours exhibit near-complete flow stabilization at the 3.0D location (Fig. 16e). The high-speed core remains well-defined along the centerline, while the surrounding flow achieves a more uniform velocity distribution. The recirculation zone is minimal, indicating efficient mixing and energy recovery. The flow at this stage is well-organized and less turbulent, suggesting that the control's impact has been effectively integrated into the overall flow structure. Overall, the velocity contours for the orientation two control demonstrate that while the d-shaped control initially induces significant flow separation and turbulence near the nozzle exit, the flow gradually stabilizes as it moves downstream. The high-speed jet becomes more streamlined, the recirculation zone diminishes, and the velocity distribution across the duct becomes more uniform. That indicates that orientation two control effectively enhances flow stability and energy recovery in the suddenly expanded duct.

6.2.3. *Streamline formation contours*

The streamline contours for orientation two control illustrate the flow behavior as the high-speed flow exits the convergent nozzle and expands into an abruptly expanded duct. These contours depict the streamline formation and flow patterns at five downstream locations at L/Ds = 0.5, 1.0, 1.5, 2.0, and 3.0, where D represents the nozzle exit diameter. The streamlines visualize flow separation, recirculation zones, and reattachment points, providing insights into how the d-shaped control affects the flow field in orientation 2.

At the 0.5D location (Fig. 17a), the streamline contours show significant flow separation immediately downstream of the nozzle exit. The high-speed jet exiting the nozzle interacts with the d-shaped control, causing the flow to diverge and form recirculation zones on either side of the central core. These zones are characterized by swirling streamlines, indicating the presence of vortices due to the sudden expansion and obstruction created by the control. The central core maintains high velocity while the surrounding flow remains turbulent and unorganized. At the 1.0D location (Fig. 17b), the recirculation zones expand further downstream, with the streamlines showing complex swirling patterns near the duct walls. The high-speed jet continues along the duct centerline while the flow near the walls remains disturbed. The interaction between the high-speed jet and the recirculating flow intensifies turbulence, leading to increased flow resistance and energy loss. The streamlines near the duct walls remain chaotic, indicating incomplete pressure recovery.

Streamline patterns suggest partial flow stabilization when the L/D = 1.5 location (Fig. 17c). The high-speed jet core becomes more organized while the recirculation zones near the walls diminish. The streamlines align more uniformly, reflecting reduced turbulence and improved flow recovery. The transition from chaotic to organized flow indicates that the flow is gradually adapting to the expanded duct geometry and the presence of the d-shaped control. The streamline contours exhibit further stabilization at the 2.0D location (Fig. 17d), with reduced recirculation zones and more streamlined flow paths. The high-speed jet along the centerline remains prominent, while the surrounding flow achieves a more uniform structure. The streamlines near the duct walls

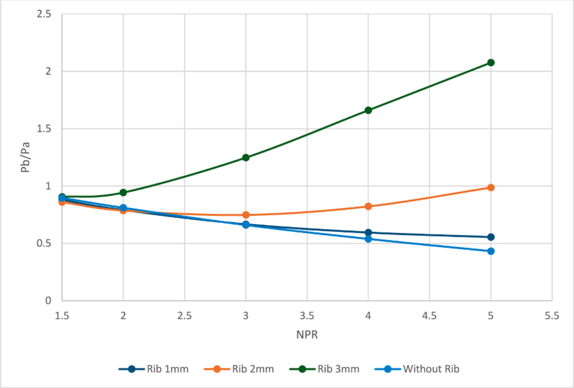

(a) L/D = 2

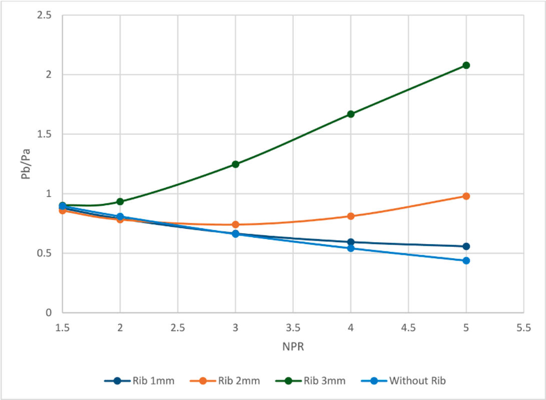

(b) L/D = 3

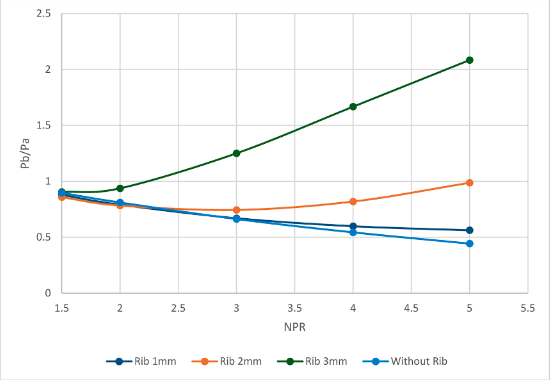

(c) L/D = 4

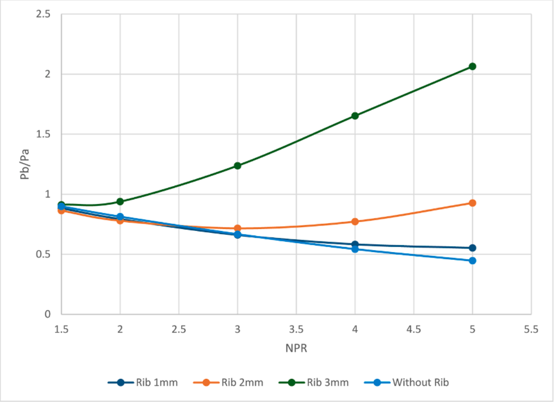

(d) L/D = 5

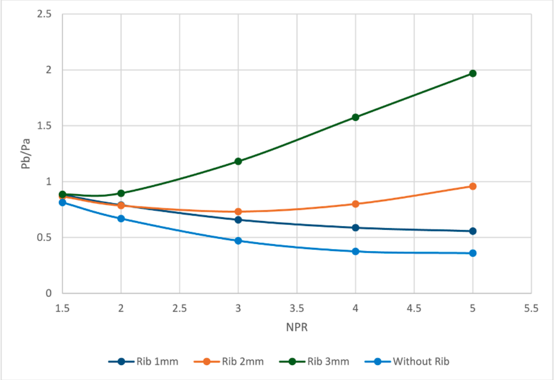

(e) L/D = 6

Fig. 19. Base Pressure Vs. NPR for numerous ducts.

become smoother, indicating improved pressure recovery and reduced energy loss. The formation of vortices weakens, suggesting that the influence of the d-shaped control is gradually diminishing downstream.

Lastly, the streamline contours show near-complete flow stabilization at the 3.0D location (Fig. 17e). The high-speed jet remains well-defined along the duct centerline, while the surrounding flow achieves a more uniform velocity distribution. The recirculation zones are minimal, and the streamlines align closely with the duct walls, indicating efficient flow recovery and reduced turbulence. The flow at this stage is well-organized, suggesting that the control's impact has been effectively integrated into the overall flow structure. Overall, the streamline contours for orientation two control demonstrate that while the d-shaped control initially induces significant flow separation and turbulence near the nozzle exit, the flow gradually stabilizes downstream. The recirculation zones shrink, the streamlines become more organized, and the overall aerodynamic efficiency improves. That highlights the effectiveness of the orientation two control in enhancing flow stability and energy recovery in the suddenly expanded duct.

6.2.4. Base pressure results when rib is located at L/D = 0.5

Fig. 18((a) to (f)) show the base pressure findings for rib setting at L/D = 0.5 for NPRs in the vary between from 1.5 to 5 for duct lengths L/D = 1 to 6 for three rib radius 0.5 mm, and 1.5 mm. The base pressure results for this rib location will differ from the other rib locations since this location is closer to the base recirculation region. Flow exits from the nozzle and is not yet stabilized. Moreover, the duct length $L = 1D$ is exposed to ambient conditions, which will control the magnitude of the pressure in the recirculation zone. Therefore, the authors feel that it is not advisable to take a call for the design of aerospace vehicles. As seen from Fig. 19(a) for the 0.5 mm rib radius, the decreasing pattern of the base pressure continues for the entire range of the NPRs. Nevertheless, despite the decreasing trend, base pressure values are still nearly fifty

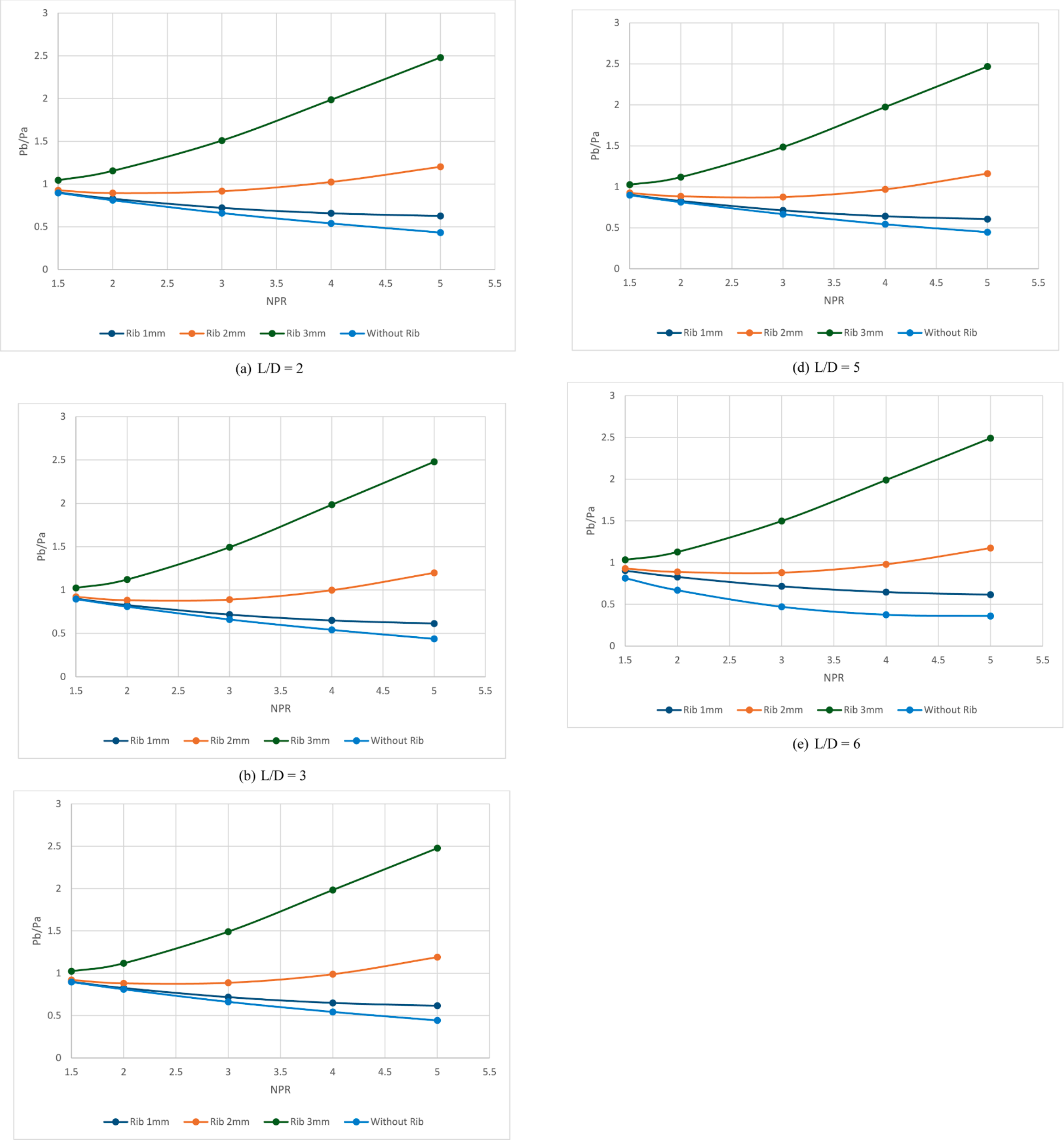

(a) L/D = 2

(d) L/D = 5

(b) L/D = 3

(e) L/D = 6

(c) L/D = 4

Fig. 20. Base Pressure Vs. NPR for numerous ducts.

percent higher than for cases without control. Hence, if the users are required to increase the base pressure marginally, say by 20 to 30%, regarding values in the non-existence of the rib, then this geometry may be the right choice.

When we look at the base pressure findings for a 1 mm radius, the trend declines until NPR =3. Once the level of the under-expansion ratio is 1.5, the declining course of the base pressure is reversed for NPR greater than 3, and the base pressure ratio value is 0.8. The base pressure is deficient by 20 %. Meanwhile, for a 1.5 mm radius, the base pressure increases progressively once the nozzle reaches the critical condition. This rib attains a base pressure ratio of 1.5, which means that using this rib, one can achieve a base pressure value of 50% more than ambient atmospheric pressure. When we explore the base pressure results for higher duct-to-length ratios like L/Ds = 2, 3, 4, 5D, and 6, they show similar negligible variations in the base pressure owing to the influence of duct dimension, rib location, and back pressure.

6.2.5. *Base pressure results when rib is located at L/D = 1*

For different NPRs and duct lengths, Fig. 19((a) to (e)) displays the base pressure findings for rib positions at 1D For rib radii 0.5 mm and 1 mm, the base pressure with and without control overlaps until NPR = 2.5. The basal pressure rises by 22 to 40 percent for the study's highest NPRs. The base pressure ratio for the 1.5 mm rib radius was as high as 2.1, and there was no trend of the base pressure diminishing; right from the study's smallest NPR, there is a positive trend of the base pressure growing. Until L/D = 5, the pattern observed for L/D = 1 appears to persist. The results for L/D = 6 are different from all other L/D values, though, for a rib radius of 0.5 mm, where the rib works for the full range of the NPRs that were examined. The results show the effect of rib position for this rib radius, and base pressure is a noticeable enhancement. The results are the same for the other rib radius. As a result, these findings are case-sensitive. The base pressure changes significantly for the lowest rib radius, whereas the results for the other two radiuses remain the same.

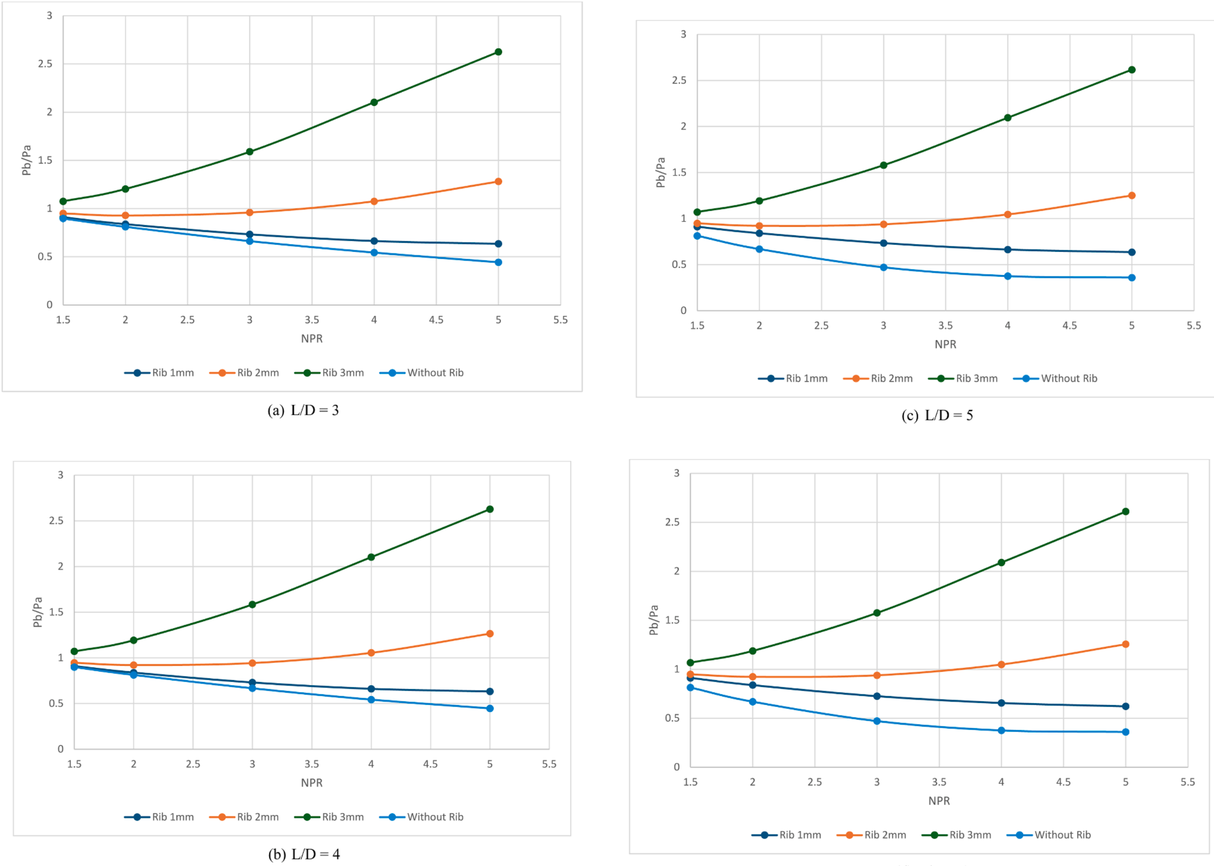

(a) L/D = 3

(c) L/D = 5

(b) L/D = 4

(d) L/D = 6

Fig. 21. Base Pressure Vs. NPR for numerous ducts.

6.2.6. *Base pressure results when rib is located at L/D = 1.5*

Fig. 20((a) to (e)) exhibits the findings of this analysis for duct lengths $L = 2D$ to 6D and the NPRs from 1.5 to 5, with a further shift in the rib position towards the downstream at L/D = 1.5. Passive control is ineffective for the lowest rib radius until the nozzle reaches critical condition, which occurs at about NPR = 2. Subsequently, an increase in NPR directs to an intensification in base pressure, according to the base pressure outcomes for L/D = 2. Nonetheless, with the maximum value of the NPR = 5, this increase is around 25%. A progressive increase in base pressure occurs when the rib radius is 1 mm immediately after NPR = 1.5. At NPR = 4, the base pressure ratio is 1.0; at NPR = 5, it is 1.2. Fig. 20(a) shows that the maximum rib radius of 1.5 mm raises the base and begins with a base pressure ratio of 1 to 2.5. Fig. 20 shows similar results for L/D = 3, 4, and 5 ((b) to (d)).

For L/D = 6, the base pressure results follow an analogous pattern, as observed when the rib is located at L/D = 1. These results can be attributed to the considerable duct length. For this combination of rib radius, rib position, and expansion levels, the field is developed so that the rib becomes effective for the entire range of the NPRs.

6.2.7. *Base pressure results when rib is located at L/D = 2*

When the passive control in the form of the d-shaped rib is placed at L/D = 2, the base pressure results as a function of the nozzle pressure ratio for duct lengths $L = 3D$, 4D, 5D, and 6D are shown in Fig. 21((a) to (d)). The base pressure shows a downward trend up to the minimum rib radius and when the control is absent. On the other hand, as the NPR values rise, the control efficacy also rises, suggesting that the under-expansion level increases in tandem with it. These results confirm that control becomes active, passive, or successful when the nozzles encounter a favorable pressure gradient. As shown in Fig. 21(a), the base pressure ratio remains unchanged for a rib radius of 1 mm, but when NPR = 5, it slightly changes for a rib radius of 1.5 mm. Findings for the subsequent duct length L/D = 4 are comparable. That was expected since L/D = 3 is the projected reattachment point. The duct length-to-diameter ratios are also 3 to 4. Therefore, the stream area of the duct will also be influenced by these two duct backpressure lengths.

For ducts, L/D = 5 and 6, the base pressure for the smallest rib radius of 0.5 mm has a different pattern than the lower L/D ratios, namely 3 and 4. A decreasing trend in the base pressure is seen for both 0.5 mm rib radii and without any control. Nevertheless, control continues to be effective for all the NPRs of the current analysis, and for the other two rib radii, there are no variations for these two ducts, L/D = 5 and 6.

6.2.8. *Base pressure results when rib is located at L/D = 3*

When the rib is located at L/D = 3, the base pressure ensuing from this study for various NPRs and L/D = 4, 5, and 6 are shown in Fig. 22 ((a) to (c)). Fig. 22(a) shows the findings of this study for L/D = 4, as seen earlier, for the lowest radius of the study up to NPR = 2, and the control is not adequate. Once the nozzle attains critical conditions, there is a continuous improvement in the control effectiveness, and for the other two radii, the control does not result in any increase. It remains the same as was seen for the previous rib locations. Hence, these results reaffirm that rib location and geometry are successful up to specific values. Later, any geometry or location change will not yield any beneficial results. Similar results are seen for L/D = 5 and 6, as seen in graphs 22 ((b) to (c)). It is found that there is a substantial change in the base pressure pattern for the smallest rib radius, and for the continuing rib radius, the base pressure results remain unchanged. These results reiterate that they are case-sensitive and must be analyzed case-to-case. These results can not be generalized.

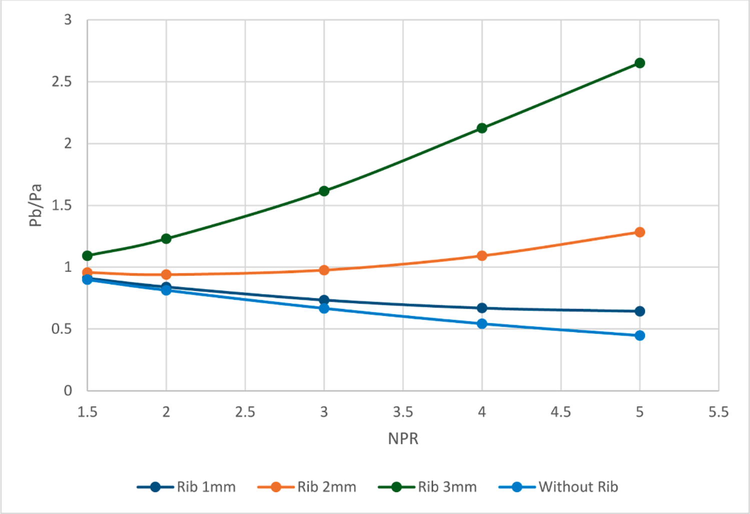

(a) L/D = 4

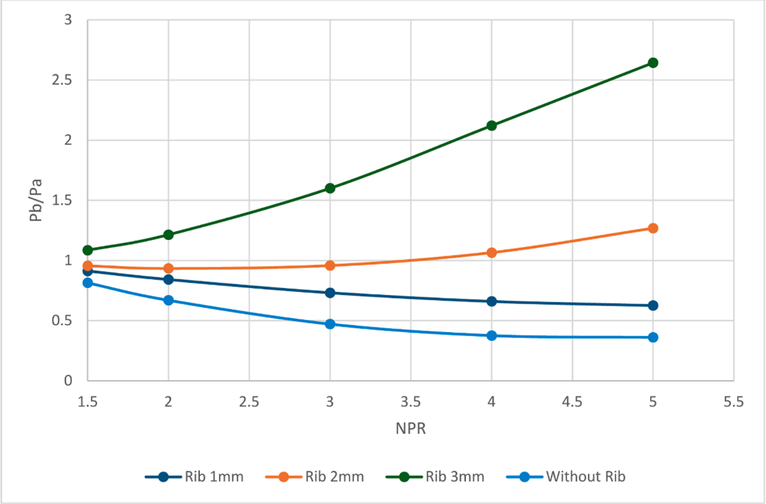

(b) L/D = 5

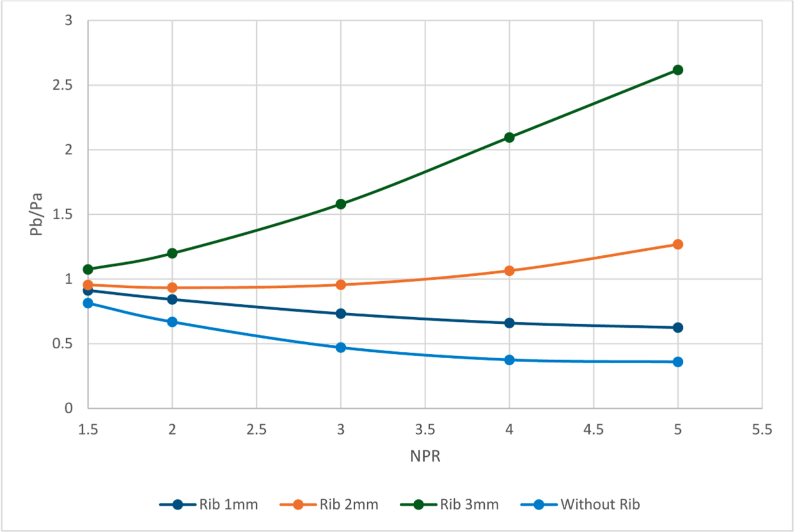

(c) L/D = 6

Fig. 22. Base Pressure Vs. NPR for different ducts.

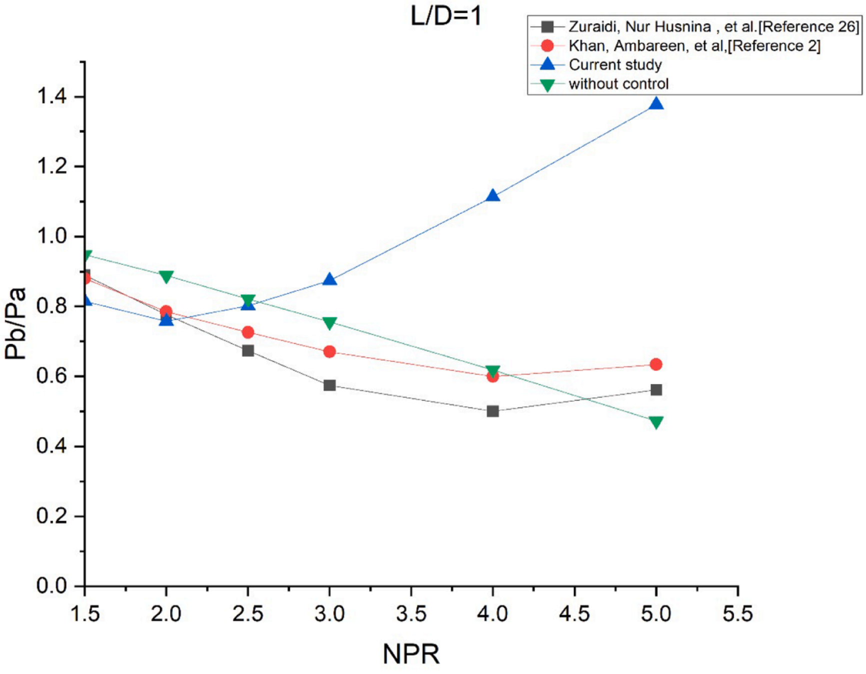

(a)

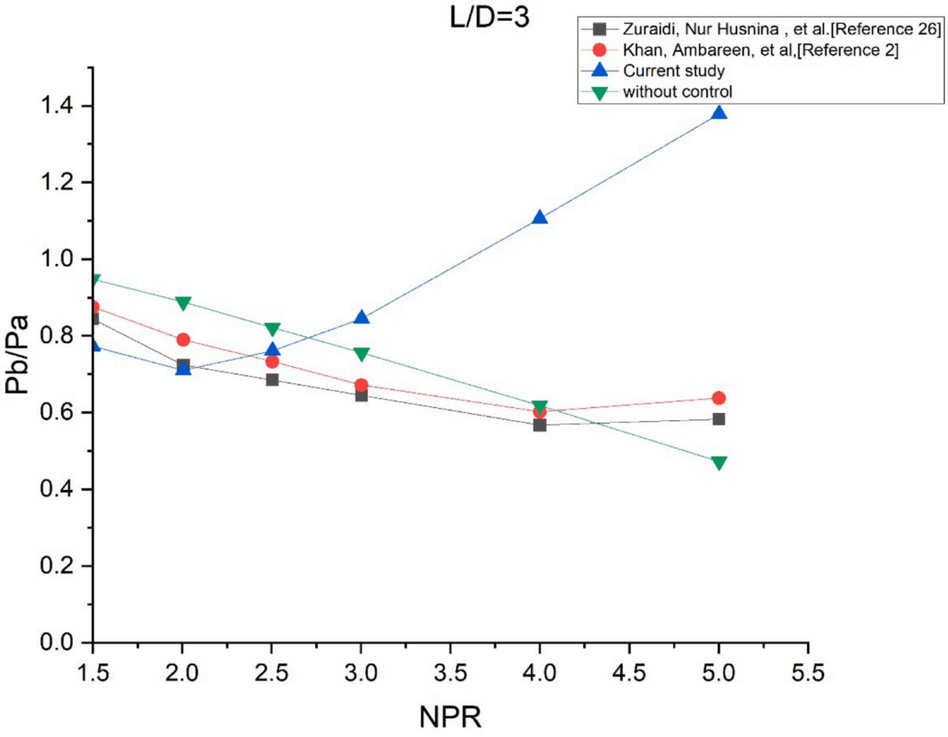

(b)

Fig. 23. Comparison of Base Pressure Results with the Existing Literature.

6.3. Comparison of base pressure results with the existing literature

Fig. 23((a) to (b)) show a comparison of the base pressure for various shapes of the ribs (e.g., a rectangular rib, a quarter circle rib, and a d-shaped rib) for L/D = 1 and 3, keeping a rib aspect ratio of 3:3. From these figures it is seen that in the absence of rib, there is a continuous decrease in the base pressure even though the nozzle has attained the critical conditions at NPR = 2, for NPRs beyond two the nozzle, is under the influence of favorable pressure gradient (i.e. nozzle is under-expanded). This declining trend in the base pressure is also against the general trends researchers have found while dealing with the control of the flow, either active or passive; in both situations, the control mechanism becomes effective once the nozzles are flowing under the influence of the favorable pressure gradient, nozzles are under-expanded (i.e., $P_e/P_a > 1$) It is imperative to understand the physics underlying this trend to understand its declining base pressure trend. It can be stated that the flow from the nozzle discharged into the expanded duct tends to connect with a reattachment length other than the ideal for a strong vortex at the base when the relief effect caused by the rise in the area ratio is over a specific limit. This mechanism renders the NPR effect on base pressure negligible for a higher area ratio. Therefore, the declining trend in the base pressure is primarily due to the higher duct diameter. However, from the literature, it is found that the decreasing trends in the base pressure are reversed for lower duct diameter. From Fig. 23((a) and (b)), it is seen that the d-shaped rib is very effective in raising the base pressure, whereas the other two ribs with a rectangular and quarter-circle are marginally effective. Therefore, a d-shaped rib seems to be the best choice for lowering the base suction and the base drag.

7. Conclusions

Because of the above discussion, we may conclude that the base pressure is decisive for NPR, area ratio, L/D ratio, rib location, and rib geometry. When the rib is kept at orientation 1, the curved part is towards the base region for various rib locations from 0.5D, 1D, 1.5D, 2D, and 3D For all the duct lengths up to $L = 1$ D to 5D, 1 mm and 2 mm ribs are ineffective; 3 mm rib is adequate, and the maximum base pressure ratio achieved is 1.4. However, for L/D = 6, the pattern for 1 mm and 2 mm is different due to the large duct and backpressure being unable to impact the flow. There is a significant change in the base pressure for a 3 mm rib. The maximum base pressure achieved remains constant. It does not change at other rib locations. Some variations exist for 1 mm and 2 mm ribs, and control effectiveness is lost whenever the duct L/D ratio is 5 or 6. Similar results and patterns are seen for rib locations of L/D = 1.5, 2, and 3.

For orientation two, the base pressure results are almost on similar lines. For the lowest rib location, L/D = 0.5, as the rib is near the base region and flow has not developed completely, the enormous achievement in the base pressure is accomplished for the rib location at L/D = 1. For other rib locations, changes in the base pressure are seen for 1 mm, and 2 mm ribs are marginal only, and some peculiar trend is seen more so for 1 mm as this rib dimension is most vulnerable for the rib locations. It is also seen that the decreasing trend in base pressure revisits whenever duct L/D is in the range of 5 to 6. This trend reiterates the influence of area ratio, where an increase in NPR is ineffective, and control does not influence the flow field despite nozzles flowing under the influence of a favorable pressure gradient. The magnitude of the base pressure for a 3 mm rib is marginally more for this orientation. It may be due to the shape of the rib facing the region. In this case, it is a flat surface, whereas in the former case, the base flow sees a curved surface; hence, that is the main reason for the slight variation in the base pressure magnitude. The passive control of base pressure and rib locations' impact on various duct lengths and expansion levels is demonstrated. One selects the ribs' geometry and location based on the user's requirement.

In this study, we have selected a few geometry and rib location cases to demonstrate that the d-shaped rib has the potential to control the base pressure compared to other rib shapes. However, due to the shortage of time, we could not do the simulation at a small interval for nozzle pressure ratio (NPR), rib location, and rib dimensions. If it is done at tiny intervals, for NPRs, rib geometry and rib placements inside the duct will yield some interesting results. Later, based on this data, we can derive some correlations that will be very useful for the future design of rockets, missiles, and launch vehicles.

Brief future work discussions should include the following:

a. Investigating the interaction between rib geometry and nozzle pressure ratio (NPR) better to understand their combined effect on base pressure regulation.

   Response: This study is limited to the sonic Mach number. In future studies, we can simulate various Mach numbers and the area ratio to give a complete picture of the passive control efficacy and its dependency on NPR, L/D ratio, and various rib geometries.

b. Exploring the impact of rib shapes other than d-shaped configurations to generalize findings across different geometries.

   Response: As of now, we can compare the influence of rib shapes on base pressure and their dependency on Mach number, L/D ratio, and NPR.

c. Conducting three-dimensional simulations or experiments to capture more complex flow phenomena that may not be fully represented in a two-dimensional analysis (e.g., https://doi.org/10.1063/5.0220149).

CRediT authorship contribution statement

Mayur Bharatbhai Makwana: Methodology, Investigation, Conceptualization. **Sayed Ahmed Imran Bellary:** Supervision, Resources, Investigation. **Sher Afghan Khan:** Writing – original draft, Methodology, Data curation. **Abdul Aabid:** Writing – original draft, Methodology, Formal analysis. **Muneer Baig:** Writing – review & editing, Funding acquisition, Formal analysis.

Declaration of competing interest

The authors declare that they have no known competing financial interests or personal relationships that could have appeared to influence the work reported in this paper.

Acknowledgment

This research is supported by the Structures and Materials (S&M) Research Lab of Prince Sultan University, and the authors acknowledge Prince Sultan University's support in paying the article processing charges (APC) for this publication.

Data availability

Data will be made available on request.

References

[1] A. Khan, A. Aabid, S.A. Khan, M.N. Akhtar, M. Baig, Comprehensive CFD analysis of base pressure control using quarter ribs in sudden expansion duct at sonic mach numbers, Int. J. Thermofluids 24 (2024) 100908, https://doi.org/10.1016/j.ijft.2024.100908. Oct.

[2] A. Khan, S.A. Khan, V. Raja, A. Aabid, M. Baig, Effect of ribs in a suddenly expanded flow at sonic mach number, Heliyon. 10 (9) (2024) e30313, https://doi.org/10.1016/j.heliyon.2024.e30313.

[3] N. Husnina, M. Zuraidi, S.A. Khan, A. Aabid, M. Baig, Passive control of base pressure in a converging-diverging nozzle with area ratio 2.56 at mach 1.8, Fluid Dyn. Mater. Process. 19 (3) (2023) 1–20, https://doi.org/10.32604/fdmp.2023.023246.

[4] A. Khan, S.A. Khan, M.N. Akhtar, A. Aabid, M. Baig, Base pressure control with semi-circular ribs at critical mach number, Fluid Dyn. Mater. Process. 22 (2024), https://doi.org/10.32604/fdmp.2024.049368.

[5] A. Aabid, A. Afifi, F.Ahmed Ghasi Mehaboob Ali, M.Nishat Akhtar, S.Afghan Khan, CFD analysis of splitter plate on bluff body, CFD Lett 11 (2019) 25–38.

[6] V. Sethuraman, P. Rajendran, S.A. Khan, A. Aabid, M. Baig, Control of nozzle flow using rectangular ribs at sonic and supersonic mach numbers, Fluid Dyn. Mater. Process. 22 (2024) 1–20, https://doi.org/10.32604/fdmp.2024.049441.

[7] M. Kadivar, D. Tormey, G. McGranaghan, A comparison of RANS models used for CFD prediction of turbulent flow and heat transfer in rough and smooth channels, Int. J. Thermofluids 20 (2023) 100399.

[8] F. Orlandi, L. Montorsi, M. Milani, Cavitation analysis through CFD in industrial pumps: a review, Int. J. Thermofluids 20 (2023) 100506.

[9] N. Bordoloi, K.M. Pandey, M. Ray, K.K. Sharma, Impact of passive fuel injections techniques in the flow field of the scramjet combustor, Int. J. Thermofluids 16 (2022) 100225.

[10] N.K. Gahlot, G.P. Bagri, R.K. Saluja, N. Singh, S. Chalia, Effect of turbulence modeling on the performance of mixed compression supersonic air intake, Authorea (2024) 1–10.

[11] T. Ambo, L. Chen, T. Nonomura, K. Asai, Effect of boattail angle on pressure distribution and drag of axisymmetric afterbodies under low-speed conditions, Trans. Jpn. Soc. Aeronaut. Space Sci. 62 (2019) 219–226.

[12] P. Viswanath, Flow management techniques for base and afterbody drag reduction, Prog. Aero. Sci. 32 (1996) 79–129.

[13] A.K. Perry, An Investigation into the Base Pressure of Simplified Automotive Squareback Geometries, Loughborough University, 2016.

[14] S. Aradag, K.A. Gelisli, E.C. Yaldir, Effects of active and passive control techniques on mach 1.5 cavity flow dynamics, Int. J. Aerospace Eng. 2017 (2017).

[15] S.M. Mousavi, E. Roohi, Three-dimensional investigation of the shock train structure in a convergent-divergent nozzle, Acta Astronaut 105 (1) (2014) 117–127, https://doi.org/10.1016/j.actaastro.2014.09.002.

[16] G.R. Rao, U.S. Ramakanth, A. Lakshman, Flow analysis in a convergent-divergent nozzle using CFD, Int. J. Res. Mech. Eng. 1 (1) (2013) 136–144.

[17] N.A. Najar, D. Dandotiya, F.A. Najar, Comparative analysis of K-ε and Spalart-Allmaras turbulence models for compressible flow through a convergent-divergent nozzle, Int. J. Eng. Sci. 2 (8) (2013) 8–17.

[18] F.J. Salvador, D. Jaramillo, J.V. Romero, M.D. Roselló, Using a homogeneous equilibrium model for the study of the inner nozzle flow and cavitation pattern in convergent-divergent nozzles of diesel injectors, J. Comput. Appl. Math. 309 (2) (2017) 630–641, https://doi.org/10.1016/j.cam.2016.04.010.

[19] B.V. Pushpa, M. Sankar, F. Mebarek-Oudina, Buoyant convective flow and heat dissipation of Cu–H2O nanoliquids in an annulus through a thin baffle, J. Nanofluids 10 (2) (2021) 292–304, https://doi.org/10.1166/jon.2021.1782.

[20] R. Koomullil, B. Soni, R. Singh, A comprehensive generalized mesh system for CFD applications, Math. Comput. Simul. 78 (5–6) (2008) 605–617, https://doi.org/10.1016/j.matcom.2008.04.005.

[21] S. Marzougui, F. Mebarek-Oudina, M. Magherbi, A. Mchirgui, Entropy generation and heat transport of Cu–water nanoliquid in the porous lid-driven cavity through a magnetic field, Int. J. Numer. Methods Heat. Fluid. Flow. (2021), https://doi.org/10.1108/HFF-04-2021-0288.

[22] K.M. Pandey, E. Rathakrishnan, Annular cavities for base flow control, Int. J. Turbo Jet Engines 23 (2) (2006) 113–128, https://doi.org/10.1515/TJJ.2006.23.2.113.

[23] J. Tu, G.H. Yeoh, C. Liu, Computational Fluid Dynamics: A Practical Approach, Butterworth-Heinemann, 2018.

[24] P.H. Oosthuizen, W.E. Carscallen, Introduction to Compressible Fluid Flow, 2nd ed., CRC Press, 2014 https://doi.org/10.1201/b15414.

[25] E. Rathakrishnan, Effect of ribs on suddenly expanded flows, AIAa J. 39 (7) (2001) 1402–1404, https://doi.org/10.2514/2.1447.